

Spiral Arms in Disks: Planets or Gravitational Instability?

Ruobing Dong¹, Joan R. Najita² & Sean Brittain^{3,2}

ABSTRACT

Spiral arm structures seen in scattered light observations of protoplanetary disks can potentially serve as signposts of planetary companions. They can also lend unique insights into disk masses, which are critical in setting the mass budget for planet formation but are difficult to determine directly. A surprisingly high fraction of disks that have been well-studied in scattered light have spiral arms of some kind (8/29), as do a high fraction (6/11) of well-studied Herbig intermediate mass stars (i.e., Herbig stars $> 1.5M_{\odot}$). Here we explore the origin of spiral arms in Herbig systems by studying their occurrence rates, disk properties, and stellar accretion rates. We find that two-arm spirals are more common in disks surrounding Herbig intermediate mass stars than are directly imaged giant planet companions to mature A and B stars. If two-arm spirals are produced by such giant planets, this discrepancy suggests that giant planets are much fainter than predicted by hot start models. In addition, the high stellar accretion rates of Herbig stars, if sustained over a reasonable fraction of their lifetimes, suggest that disk masses are much larger than inferred from their submillimeter continuum emission. As a result, gravitational instability is a possible explanation for multi-arm spirals. Future observations can lend insights into the issues raised here.

Subject headings: protoplanetary disks — planets and satellites: formation — planet-disk interactions — stars: pre-main sequence — stars: variables: T Tauri, Herbig Ae/Be — stars: pre-main sequence

¹Steward Observatory, University of Arizona, 933 N Cherry Ave, Tucson, AZ 85721, USA, rdong@gmail.com

²National Optical Astronomical Observatory, 950 North Cherry Avenue, Tucson, AZ 85719, najita@noao.edu

³Department of Physics & Astronomy, 118 Kinard Laboratory, Clemson University, Clemson, SC 29634-0978, USA, sbritt@clemson.edu

1. Introduction

As the birthplaces of planets, protoplanetary disks surrounding young stars lend unique insights into the circumstances under which planets form. The initial masses of disks set an upper limit on the mass budget for planet formation, a basic constraint on theories of how planets form. From the detailed study of disk morphologies, we may also glean evidence of the formation of planets themselves, e.g., from the detection of gaps, rings, and spiral arms created by planets. As a result, numerous studies have examined the protoplanetary disks around T Tauri stars and Herbig stars for clues to their structure and planet formation status.

Despite their fundamental importance, disk masses have been proven difficult to measure. Although disk masses are commonly inferred from submillimeter continuum fluxes, which probe the dust content of disks, several arguments strongly suggest that much of the solids in T Tauri disks have grown beyond the sizes probed by submillimeter continua. As one simple example, submillimeter continuum disk masses are too low to even account for the solids that are known to be locked up in exoplanet populations and debris disks, indicating that T Tauri disks harbor more massive reservoirs of solids than those probed by continuum measurements (Najita & Kenyon 2014), and disk masses are underestimated as a result.

More graphically, high resolution submillimeter continuum images of disks made with ALMA commonly show stunning rings and gaps (ALMA Partnership et al. 2015; Andrews et al. 2016; Cieza et al. 2016; Isella et al. 2016; Cieza et al. 2017; Loomis et al. 2017; Fedele et al. 2018; Huang et al. 2018; Dipierro et al. 2018), structures that signal that disk solids have grown beyond centimeter sizes and possibly into planetary mass objects (e.g., Dong et al. 2015c; Dipierro et al. 2015; Dong et al. 2017a; Bae et al. 2017). These results exclaim that disks are highly evolved and call into question disk mass estimates made under the usual assumption of simple, unevolved, optically thin disks. Given the difficulty of measuring disk masses through proxies such as dust continuum emission, other approaches are welcome.

Alongside these developments, high contrast images of disks made in scattered light also reveal remarkable features. Near-infrared scattered light imaging observations probe the spatial distribution of small grains, approximately micron-sized or smaller, that are well-coupled to the gas (Zhu et al. 2012; Pinilla et al. 2012). These studies have revealed spiral arms in a growing number of disks (Figure 1), both prominent near-symmetric two-arm spirals (e.g., Grady et al. 2013; Benisty et al. 2015) and more flocculent multi-arm spirals on smaller scales and at lower contrast (e.g., Fukagawa et al. 2004; Hashimoto et al. 2011). Spiral arms can be produced by either gravitational instability (e.g., Rice et al. 2003; Lodato & Rice 2004; Stamatellos & Whitworth 2008; Kratter et al. 2010; Kratter & Lodato 2016) or the presence of massive companions (gas giant to stellar masses; e.g., Kley & Nelson 2012;

Zhu et al. 2015; Muñoz & Lai 2016).

The presence or absence of spiral arms in disks, if induced by gravitational instability, can place a dynamical constraint on disk masses. Gravitational instability occurs when the destabilizing self-gravity of a disk dominates over the restoring forces of gas pressure and differential rotation (Toomre 1964; Goldreich & Lynden-Bell 1965), a requirement that roughly translates into $M_{\text{disk}}/M_{\star} \gtrsim 0.1$ under typical conditions (Kratte & Lodato 2016). Spiral arms induced by gravitational instability are expected to appear nearly symmetric in scattered light imaging, with the number of arms roughly scaling as $n \approx M_{\star}/M_{\text{disk}}$ (Lodato & Rice 2004, 2005; Cossins et al. 2009; Dong et al. 2015a).

Planetary companions can also drive spiral arms (Goldreich & Tremaine 1979; Ogilvie & Lubow 2002). A massive companion (above a few $\times 10^{-3}M_{\star}$) generates a set of near-symmetric two-arm spirals interior to its orbit, similar to the morphology of observed two-arm spirals (Dong et al. 2015b, see also Fig. 2a,b), with the companion located at the tip of the primary arm (e.g., Zhu et al. 2015; Fung & Dong 2015; Bae et al. 2016). Lower mass companions ($\sim 10^{-3}M_{\star}$) may generate additional arms interior to their orbits, weaker than the primary and secondary arms in scattered light (e.g., Juhász et al. 2015; Fung & Dong 2015; Lee 2016; Bae et al. 2017; Bae & Zhu 2018, see also Fig. 2d,e). If spiral arms are driven by planets, arm morphologies can provide clues to the location and masses of the planets.

Here we explore these hypotheses for the origin of the spiral arms detected in scattered light by comparing (*i*) the demographics of arm-bearing disks (disk masses and stellar accretion rates) with those of other young stars and (*ii*) the incidence rate of arms compared to that of resolved planetary companions to mature stars. Although we begin by considering the detection rates of spiral arms in disks surrounding both T Tauri stars and Herbig stars, we end up focusing more closely on the properties of the higher mass Herbig stars, where the census of scattered light structures is more complete.

In §2 we characterize the occurrence rate of spiral arm structures in scattered light imaging of disks. To explore whether spiral arms could be produced by orbiting companions, we compare in §3 the occurrence rates of spiral arms in disks to that of giant planetary companions to mature stars. In §4 we explore the alternative possibility that spiral arms are driven by gravitational instability by examining the masses of disks that show spiral arm structures, as probed by submillimeter continuum emission and stellar accretion rates. In §5 we examine the planet and gravitational instability hypotheses in greater detail before suggesting scenarios that are potentially consistent with our results. We summarize our results in §6, where we also describe future studies that can lend insights into the issues raised here.

2. Sample Selection and Statistics

In near-infrared scattered light imaging of disks, spiral arms have been found in both embedded Class 0/I objects surrounded by infalling envelopes (Canovas et al. 2015; Liu et al. 2016b) and revealed Class II objects (i.e., Herbig and T Tauri stars; Figure 1). While gravitational instability may drive the arms in Class 0/I disks (e.g., Vorobyov & Basu 2005, 2010; Tobin et al. 2016; Pérez et al. 2016; Dong et al. 2016b; Tomida et al. 2017; Meru et al. 2017), which tend to be massive and are fed by infall from the envelope, the origin of the arms detected in Class II disks is unclear.

Figure 2 shows how in principle spiral arms could serve as signposts of either an orbiting planet or a gravitationally unstable disk. The left column shows observed images of two representative disks: MWC 758, with its prominent near-symmetric two-arm spirals (Fig. 2a); and HD 142527, with multiple small-scale, lower contrast arms (Fig. 2d). The middle and right columns show synthetic observations from the literature, produced in combined hydrodynamic and radiative transfer simulations, which illustrate how morphologically similar spiral structures can occur in disks with orbiting planets (middle column) or when a disk is gravitationally unstable (right column). As discussed in §1, both a multi-Jupiter mass giant companion and a gravitationally unstable disk with $M_{\text{disk}} \sim 0.5M_{\star}$ can produce a set of prominent two-arm spirals (Fig. 2b,c), while lower mass planets ($M_{\text{p}} \sim M_{\text{J}}$) and marginally gravitationally unstable disks with $M_{\text{disk}} \sim 0.1M_{\star}$ can produce multiple small-scale arms at low contrast (Fig. 2e, f).

To attempt to distinguish between these two scenarios for the origin of spiral structure in disks, we first characterize, in this section, the occurrence rate of spiral arms in scattered light imaging of disks. §2.1 describes the data available and our process of selecting a sample of disks well studied in scattered light that are suitable for our study. The occurrence rate of arms within this sample is described in §2.2. Because the sample of well-studied disks is small in size, in §2.3 we examine the occurrence rate of arms within in a volume-limited sample of Herbig stars, which provides a lower limit on the true occurrence rate.

2.1. Disk Imaging Sample

We collected from the literature a sample of protoplanetary disks that have been spatially resolved in scattered light at optical to NIR wavelengths (Appendix Table A.1.1) and that meet four main criteria. First, the disk is gas-rich (i.e., debris disks are excluded). Second, the disk was observed with an inner working angle $< 1''$, small enough to reveal the inner ~ 100 AU planet forming region (most disks imaged to date are 100–200 pc away).

Third, the disk surface was revealed with sufficient signal-to-noise to identify possible structures. Finally, the disk was observed with an angular resolution $\lesssim 0''.1$ in order to detect and resolve spiral arms.

The third condition largely restricts the sample to Class II objects without a substantial envelope, as the disk surface of more embedded sources is often not accessible in scattered light. It also excludes disks that are completely flat or shadowed (Dullemond & Dominik 2004). The last criterion restricts the sample to those observed at L -band ($3.8 \mu\text{m}$) or shorter wavelengths, because $\lambda/D \lesssim 0''.1$ requires $\lambda \lesssim 3.8 \mu\text{m}$ for observations made with $D \approx 8 \text{ m}$ diameter telescopes. Systems that have been directly imaged, both with and without a coronagraphic mask, are included, whereas interferometric observations are not. The resulting sample of 49 objects (Table A.1.1) derives mainly from a few major exoplanet and disk surveys, such as the Subaru-based SEEDS (Tamura 2009; Uyama et al. 2017) and the VLT-based SHINE surveys, supplemented by studies of smaller samples that used a variety of ground-based instruments and *HST*. Roughly half of the sources are transitional disks (i.e., disks whose inner region is optically thin in the continuum; Espaillat et al. 2014).

We further removed sources viewed at high inclination ($\gtrsim 70^\circ$) whose scattered light structures may be difficult to assess (AK Sco, T Cha, AA Tau, RY Lup, HH 30, HK Tau, HV Tau C, LkH α 263C, and PDS 144N). It is possible to identify spiral arms in disks at such high inclinations (e.g., RY Lup; Langlois et al. 2018); however it is usually a challenge because of the resulting geometric effect (Dong et al. 2016a). We also excluded any remaining Class 0/I sources and sources undergoing accretion outbursts (FU Ori, HL Tau, R Mon, V 1057 Cyg, V1735 Cyg, and Z CMa) in order to probe a restricted evolutionary state and to avoid scattered light contamination from an infalling envelope.

Sources with known stellar companions within $5''$ (HD 100453, GG Tau, HD 150193, and T Tau) were also excluded to avoid systems in which a stellar companion induces disk structure. Whereas a massive planet exterior to the arms can generate the observed two-arm spirals, a stellar companion closer than $\sim 5''$ could produce similar spiral structure in a disk with a typical size of $\sim 1\text{--}2''$; (e.g., as in the case of the HD 100453 disk; Wagner et al. 2015; Dong et al. 2016c; Wagner et al. 2018). The companion to HD 142527, which is located well within the gap in the disk, is commonly interpreted as having too low a mass ($0.13M_\odot$; Lacour et al. 2016) and eccentricity to generate the observed spiral arms, so this object is included in our sample (although see Price et al. 2018). Lastly, we removed HD 141569 from the sample, because its low dust mass (on the order of $1 M_\oplus$ or less; Flaherty et al. 2016; White et al. 2016) makes the system prone to radiation pressure and photoelectric instability, which can also produce spiral arm structures (e.g., ?).

Finally, we arrive at a sample of 29 “well-studied NIR disks”, whose stellar and disk

properties are listed in Table 1. The tabulated M_\star values were obtained from T_{eff} and L_\star using the Siess et al. (2000) pre-main-sequence evolutionary tracks. Notes on individual sources are provided in Appendix §D. The final sample contains 11 Herbig sources (the first 11 rows in the table) and 18 T Tauri stars. Of the 29 sources, 8 have spiral arms: the MWC 758, SAO 206462, LkH α 330, and DZ Cha disks show prominent two-arm spirals (Fig. 1, top), the AB Aur, HD 142527, and HD 100546 disks show multiple small arms, and the V1247 Ori disk has one arm (Fig. 1, bottom).

2.2. Spiral Arm Statistics Among Well-studied NIR Disks

From the results shown in Table 1, we find that the incidence rate of spiral arms in disks is surprisingly high among young well-studied A and B stars (3/7), well-studied FGK stars (5/22), and well-studied disks overall (8/29; Table 3).

We can make a similar accounting of spiral fraction by stellar mass rather than by spectral type. Anticipating our comparison of the spiral arm incidence rate to that of massive companions to mature AB stars (§3), we define a Herbig intermediate mass star (IMS) sample over a broader range of spectral type. A main sequence F0 star has a mass of $\sim 1.5M_\odot$ (e.g., Pecaat & Mamajek 2013). So we consider as Herbig IMS all Herbig systems with spectral types between F6 and B9, and stellar masses $> 1.5M_\odot$.

Table 3 shows that the spiral fraction is 6/11 among well-studied Herbig IMS and 2/18 among the low mass stars (LMS) that make up the rest of the sample. The incidence rate of two-arm spirals is also high: 2/11 among the well-studied Herbig IMS and 2/18 among the LMS. Although the samples are small, the data can nevertheless lend insight into whether there is a significant difference between the occurrence rates of spiral structure in LMS and Herbig IMS disks. For example, using Fisher’s exact test (a contingency table analysis), we find that there is a 3% probability (two-tailed p-value) that the spiral occurrence rate among Herbig IMS is the same as that among low mass stars. Thus the apparent low occurrence rate of spirals among low mass stars compared to Herbig IMS is statistically significant (see also Avenhaus et al. 2018; Isella & Turner 2018).

There are a couple of biases associated with these results. Firstly, scattered light imaging studies often target sources with interesting known structures (e.g., transitional disks) and sources that appear to show interesting structures at modest signal-to-noise receive more extensive follow up. Secondly, scattered light imaging studies are only sensitive to disk structures that can be seen in scattered light. If a disk’s surface is not sufficiently flared, its spiral structure cannot be detected with this technique.

Despite these difficulties, we can obtain a lower limit on the true spiral fraction of disks by examining the fraction of disks with known spiral arms within a volume-limited sample of comparable young stellar objects. We therefore focus our study on the Herbig IMS population, because a fair fraction of such sources within the local volume have already been surveyed in scattered light. In contrast, only a small fraction of the (lower mass) T Tauri population has been studied, and as a result, a corresponding lower limit on the true spiral fraction for LMS would not be a significant constraint.

2.3. A Volume-limited Sample of Herbig Stars

Excluding V1247 Ori, which is very distant (320 pc), the remaining Herbig IMS in Table 1 are all within 200 pc. We therefore focus on a sample of Herbig IMS within this volume, i.e., Herbig sources within 200 pc that have spectral type F6 or earlier, $M_{\star} > 1.5M_{\odot}$, and no known stellar companion within $5''$.

Table 2 compiles a list of sources from the literature meeting these criteria (Walker & Wolstencroft 1988; The et al. 1994; Malfait et al. 1998; Vieira et al. 2003; Erickson et al. 2011; Chen et al. 2012). Generally, these stars are identified by their association with star forming regions or a reflection nebula and the presence of hydrogen emission lines (particularly H α). Because the sample could be useful for studies other than the one carried out here, the list also includes, for completeness, sources that we ignore in our study (indicated in Column 4 of Table 2): sources with stellar companions $0''.3$ – $5''$ away (HR 811, V892 Tau, PDS 178, CQ Tau, HD 100453, HR 5999, MWC 863, TY CrA, T CrA), sources with $M_{\star} < 1.5M_{\odot}$ (AK Sco), sources with low, potentially optically thin dust (HD 141569), and sources with decretion disks (51 Oph).

Excluding these sources, there are 24 remaining sources, which we carry forward as our “volume-limited Herbig IMS” sample. Ten of these have been well studied in NIR imaging (i.e., they are in Table 1). Note that with the above prescription for the Herbig IMS sample, we exclude younger sources such as LkH α 330 (Table 1) which also has a stellar mass $> 1.5M_{\odot}$ but a later spectral type (G3; Figure 3). These sources are excluded in part because earlier spectral type sources (F5–B9) have been studied more completely in scattered light; younger, more embedded disks are more difficult to study in scattered light due to contamination from the envelope. They are also more numerous and much less completely studied in scattered light. The masses of the later spectral type sources are more uncertain as well.

Within the volume-limited Herbig IMS sample (Table 2), 5 of the 10 well-studied sources display spiral structure (AB Aur, MWC 758, HD 100546, SAO 206462, HD 142527). The

true spiral fraction depends on whether the remaining 14 sources that have not been well studied (i.e., are not included in Table 1) have arms or not. Thus, the minimum spiral fraction is $5/24$, and the minimum two-arm spiral fraction is $2/24$ (Table 4). We conclude that even after correcting for systems that have not been studied well in scattered light, the spiral fraction of Herbig IMS is high. Detailed studies of the additional Herbig IMS within 200 pc would be extremely valuable in firming up the spiral fraction.

3. Comparison with Exoplanet Demographics

The two-arm spirals observed in scattered light can be produced by 5–13 M_J planets located 30–300 AU from the star (Fung & Dong 2015 and Dong & Fung 2017). To explore whether this scenario is tenable, we compare the incidence rate of arms with the incidence rate of planetary companions to mature A and B stars in the corresponding mass and separation range. Planetary companions to mature stars are an advantageous population to study because they are better characterized than are companions to Herbig stars and T Tauri stars (Bowler 2016).

Compiling the results of direct imaging searches for planetary companions in this mass and separation range, Bowler (2016) reported that only 3 mature (single) AB stars have such a companion out of a total sample of 110 stars with spectral types B2 to A9. This result assumes that planetary companions have the properties predicted by “hot start” models (see §5). In comparison, the two-arm spiral fraction among well-studied Herbig IMS is larger ($2/11$; §2.2). Although the number of detections is small in both cases, there is only a 6% probability of obtaining such discrepant results if the two rates are the same, according to Fisher’s exact test.

Further observations are needed to explore this possible difference. As noted in §2.3), the two-arm spiral fraction in the volume-limited Herbig IMS sample (Table 4) is at least $2/24$. If future observations show that there are no other two-arm spirals within 200 pc than the two already known, the probability that the two rates are the same would be 21% and the difference in the observed rates would be of little statistical significance. However, if two additional two-arm spirals are found in the sample, there would only be a 2% probability that the $4/24$ spiral fraction and the Bowler (2016) fraction are the same, and the difference in the rates would be quite significant.

The occurrence rate of companions to mature FGK stars is lower than that for mature AB stars (Bowler 2016). To compare with the FGK companion rate, we can select sources from Table 1 that are “future FGK stars”, i.e., sources with stellar masses between $0.5 M_\odot$

and $1.5 M_{\odot}$ (TW Hya, PDS 70, J1604-2130, RX J1615.3-3255, DoAr 28, V4046 Sgr, GM Aur, LkCa 15, PDS 66, SR 21, IM Lup, DZ Cha). The incidence rate of two-arm spirals among the well-studied “future FGK stars” is 1/12 compared with the 0/155 incidence rate of 5–13 M_J companions to mature FGK stars in the 30–300 AU separation range (Bowler 2016; Vigan et al. 2017). There is a 7% probability that the two rates are the same, similar to the situation for the higher mass stars. Further observations are needed to quantify the extent to which these rates differ.

With the apparent paucity of massive planetary companions to mature AB stars appearing to question the idea that such planetary companions drive two-arm spirals in Herbig disks, in the next section we explore the alternative possibility that spiral arms are driven by gravitational instability. We return in §5 to the planetary companion hypothesis and discuss ways in which it may be consistent with observations.

4. Disk Masses and Gravitational Instability

To help interpret the origin of the spiral arms detected in scattered light imaging, we have also compiled disk masses and stellar accretion rates for the volume-limited Herbig IMS sample (Table 2). The latter can provide a complementary estimate of disk (gas) mass assuming a typical accretion history for the disk (Hartmann et al. 1998). Tables 1 and 2 tabulate the disk dust masses M_{dust} calculated from submillimeter continuum fluxes (Appendix §B). Stellar accretion rates \dot{M}_{\star} are determined from the veiling of the Balmer discontinuity or hydrogen emission line fluxes; further details are provided in Appendix §C.

Turning first to the dust masses, although they may not be a reliable quantitative measure of disk mass (§1), they might serve as a relative measure: sources with higher disk gas masses may also have higher dust masses. Assuming $M_{\text{disk}} = 100M_{\text{dust}}$, Figure 4 shows the ratio of $M_{\text{disk}}/M_{\star}$ for all sources in the volume-limited Herbig IMS sample that have estimated dust masses. The ratio $M_{\text{disk}}/M_{\star}$ ranges from $\sim 10^{-3} - 10^{-1}$. Apart from HD 142527, which has a very large dust mass, the sources with two arms (blue bars) or multiple arms (green bars) are distributed throughout this range and interspersed with other sources, both those known to have no arms (black bars) and those that have not yet been studied in scattered light in detail (gray bars).

There is no obvious difference in the $M_{\text{disk}}/M_{\star}$ ratio of disks with and without arms. The average ratio is 0.008 for the entire volume-limited Herbig IMS sample. Sources with arms and those known to have no arms both have the same average ratio, 0.02. In other words, scattered light surveys have preferentially studied sources with higher submillimeter

continuum fluxes.

One indication that these values are flawed as quantitative measures of disk mass comes from estimating the remaining disk lifetime assuming these disk masses, $\tau_{\text{life}} = M_{\text{disk}}/\dot{M}_{\star}$. Figure 5 shows τ_{life} for sources in the volume-limited Herbig IMS sample for which both measurements are available. If we assume that the remaining disk lifetime is 2 Myr, comparable to the average age of disk-bearing young stars (Hernández et al. 2008; Richert et al. 2018) and a conservative estimate based on the HR diagram (Figure 3), half of the sources have lifetimes $\lesssim 0.2$ Myr, a mere 10% of the average age. The short lifetime is a consequence of the high accretion rates. If these values are correct, half of the Herbig stars within 200 pc are in the last 10% of their mass-building phase of life, which seems implausible.

We could instead assume that we are viewing Herbig stars on average at middle age, a current age of at least $t_0 \sim 2$ Myr. Parametrizing the decline of \dot{M}_{\star} with time as $\dot{M}_{\star}(t) = \dot{M}_{\star}(t_0)(t/t_0)^{-\eta}$ (e.g., Hartmann et al. 1998), where t_0 is the current age of the star, the total mass that the star accretes at later times $t > t_0$ is $M_{\text{disk}} = \dot{M}_{\star}(t_0)t_0/(\eta - 1)$. For $\eta \sim 1.5$ (Sicilia-Aguilar et al. 2010, Hartmann et al. 1998), $M_{\text{disk}} \sim 2\dot{M}_{\star}(t_0)t_0$. With this estimate, the average $M_{\text{disk}}/M_{\star} \sim 0.13$, about ten times higher than the disk masses estimated from submillimeter continua. If the stars are older, the implied disk masses are higher.

Figure 6 shows $M_{\text{disk}}/M_{\star}$ where M_{disk} is estimated as above. The sources with two (blue bars) or multiple arms (green bars) are concentrated in the upper half of the sample, reaching values as large as 0.6 (AB Aur), with about one-half to one-third of the sample above the nominal gravitational instability limit of $M_{\text{disk}}/M_{\star} = 0.1$. The clustering of “arm” sources toward higher $M_{\text{disk}}/M_{\star}$ would be consistent with the arms being generated through or enhanced by gravitational instability. It would be extremely interesting to measure the scattered light morphology of the unstudied sources (gray bars). If the lower mass disks also show spiral arms, it is unlikely that gravitational instability plays the major role in generating arms.

Figure 7 compares the above submillimeter continuum-based and stellar accretion-based disk masses for the volume-limited Herbig IMS sample as well as the T Tauri stars studied by Andrews & Williams (2007). Both groups of sources have, on average, 3–10 times larger masses estimated from stellar accretion rates than from dust continuum. The discrepancy between the disk masses estimated by these two methods has been previously noted for T Tauri stars by several authors (e.g., Andrews & Williams 2007; Rosotti et al. 2017). The Herbig IMS studied here show a similar trend.

5. Discussion

Among disks that have been well-studied in scattered light, spiral arm structures are surprisingly common (§2.2), although their origin is unclear. While giant planets and gravitational instability have both been put forward as explanations for the observed spiral structure, neither explanation is readily confirmed in our study. We find that despite the small sample sizes studied to date, we can infer that two-arm spirals occur more frequently among Herbig IMS disks than do massive giant planet companions to mature AB stars, challenging the planet hypothesis (§3). The viability of gravitational instability as an explanation for spiral structure is uncertain, because submillimeter continuum-based disk masses are low. However, as we showed, disk masses may be substantially larger if stellar accretion rates are a guide (§4). In this section, we examine the proposed hypotheses in greater detail before presenting scenarios that are potentially consistent with our results.

Shadows and Stellar Flybys. Spiral arms detected in scattered light have also been modeled as arising from rotating shadows cast by a warped inner disk (e.g., Montesinos et al. 2016; ?) and stellar flybys (e.g., Pfalzner 2003). These alternative explanations require specific conditions that are unlikely to be satisfied in the majority of cases. The moving shadow scenario is best at explaining grand design two-arm spirals; yet in the only disk with both a clear $m=2$ shadow pattern and a set of two-arm spirals (HD 100453), the disk’s arms are almost certainly induced by the visible stellar companion (Dong et al. 2016c; Wagner et al. 2018). To catch the spirals induced by a stellar flyby, one needs to image the system within a few dynamical times (i.e., $< 10^4$ years at typical distances) after the closest encounter before the spirals winded up due to differential rotation (Pfalzner 2003). The short timescales make it unlikely to catch the disk in this situation. Because these two options are very unlikely to be the general mechanisms responsible for observed spiral arms in scattered light, we focus more closely on the gravitational instability and planetary companion hypotheses that have been considered more intently in the recent literature.

Gravitational Instability. Exciting two-arm spirals in a gravitationally unstable disk requires $M_{\text{disk}}/M_{\star} \sim 0.5$, a situation that may occur in Herbig disks, especially if they have recently decoupled from their infalling envelopes. In such systems, spiral shocks transport angular momentum and drive rapid accretion, with $\dot{M}_{\star} \gtrsim 10^{-5} M_{\odot} \text{ yr}^{-1}$ (Kratte et al. 2008, 2010; Dong et al. 2015a). Consequently, the disk mass decreases quickly and the two-arm phase is brief (on the order of 10^4 yr). As the disk mass drops, the disk accretion rate also declines, and the disk structure shifts to a multi-arm morphology (e.g., Rice & Armitage 2009, Hall et al, in prep.). Eventually the disk is stabilized against gravitational instability and the disk settles down to an even lower accretion rate.

This scenario appears inconsistent with the demographic properties of disks with two-

arm spirals. In the above picture, two-arm spirals should occur in systems with the largest \dot{M}_* . Instead, observed two-arm spiral disks have middle-of-the-road \dot{M}_* values among the Herbig IMS within 200 pc (Figure 5). Two-arm spirals are also expected to be rare, because this phase lasts for on the order of 1% of the 2 Myr average age of disk-bearing stars once envelope infall have ceased. In contrast, two-arm spirals are found in 2/11 (or $\sim 18\%$) of the well-studied Herbig IMS and $\geq 2/24$ (or $\gtrsim 8\%$) of the volume-limited Herbig IMS sample (Table 4). Disks with two-arm spirals are also expected to be evolutionarily young, and to have just emerged from their infalling envelopes. In the HR diagram, disks with two-arm spirals are of preferentially later spectral type than other well-studied Herbig stars, but they are not preferentially younger (Fig. 3).

Although it seems unlikely to explain the two-arm spirals, gravitational instability is a possible explanation for multi-arm spirals. Disks with $M_{\text{disk}}/M_* \sim 0.1$ have multiple arms and are marginally unstable, with disk accretion rates $\sim 10^{-8}\text{--}10^{-6}M_\odot \text{yr}^{-1}$ in the outer disk (e.g., Dong et al. 2015a; Hall et al. 2016). They can remain in this state for a period $\tau \sim M_{\text{disk}}/\dot{M}_*$, or $10^5\text{--}10^7$ yr, comparable to the 2 Myr average age of disk-bearing stars. Additional disk accretion mechanisms, such as the magnetorotational instability (Balbus & Hawley 1992; Gammie 2001) or magnetized disk winds (e.g., Bai et al. 2016; Bai 2017), will become more dominant as the gravitational instability-driven accretion rate declines.

The relatively long lifetime of the multi-arm phase of gravitational instability is possibly consistent with the 3/11 (or 27%) incidence rate of multi-arm spirals among well-studied Herbig IMS and $\geq 3/24$ (or $\geq 13\%$) incidence rate within the volume-limited Herbig IMS sample (Table 4). All three of the multi-arm disks have large disk masses based on their stellar accretion rates ($M_{\text{disk}}/M_* \gtrsim 0.1$; Figure 6) as well as stellar accretion rates in the above range $\sim 10^{-8}\text{--}10^{-6}M_\odot \text{yr}^{-1}$ (Figure 5). Note that the similarity between observed stellar accretion rates and the predicted outer disk accretion rates suggest that gravitational instability-driven accretion in the outer disk could potentially be sustained down to small disk radii and onto the star; further theoretical work is needed to understand the details of the accretion process. Numerical simulations that quantify the time that a disk stays in each n -arm state in a realistic environment will be extremely useful to explore this possibility.

Planetary Companions. By studying sources that have been well studied in scattered light, we have focused on older, revealed Herbig stars that are not obscured by an infalling envelope. Thus our sample is biased against gravitational instability, which is more likely to occur in (younger) massive disks, and possibly toward giant planets, which may take a few Myr to form. It is therefore surprising to find that the properties of the sample seem inconsistent with the reported properties of giant planets around mature A stars: two-arm spirals appear to be more common than the giant planets massive enough to drive them.

One possible resolution to this discrepancy is that giant planets are fainter than we think, i.e., current direct imaging searches for planetary companions to mature A stars may underestimate the planetary masses to which they are sensitive. In converting companion fluxes (and detection upper limits) to masses, one can choose between “hot start” (e.g., COND and DUSTY models, Baraffe et al. 2003; Chabrier et al. 2000) and “cold start” evolutionary models (e.g., Fortney et al. 2008; Spiegel & Burrows 2012). The former, used by most investigators, predicts a higher luminosity for a given star at a given age with a given mass, than the latter. Neither set of models has been observationally confirmed for planetary mass objects at these young ages. Multi- M_J companions, capable of driving observed two-arm spirals, may not be detectable by current surveys if the “cold start” models are appropriate — at 50 Myr, a $3M_J$ hot start planet has roughly the same H -band luminosity as a $10M_J$ cold start planet (Baraffe et al. 2003; Spiegel & Burrows 2012). Planets that are fainter than typically assumed would also help explain why direct imaging searches for the predicted perturbers in two-arm spiral disks have failed to detect massive giant planets at the flux levels predicted by the hot start models (SAO 206462 and MWC 758; Maire et al. 2017; Reggiani et al. 2018).

As an alternative way to resolve the discrepancy, one might imagine that multi- M_J planets located at 10s to ~ 100 AU from the star may be more common at a few Myr than at the 10–100 Myr ages typically probed by direct imaging studies (e.g., Bowler 2016), either because planets migrate inward from the original orbital distances via disk-planet interactions, and/or they are scattered out of the system via planet-planet interactions. Both options appear unlikely, however. While a planet could be driven inward by an outer disk located beyond the planet (e.g., Kley & Nelson 2012), in all systems with two-arm spirals the purported planet is located *beyond* the edge of the disk. In the planet-planet interaction scenario, multiple giant planets that are initially stabilized by the gas disk (e.g., Dunhill et al. 2013) later undergo planet-planet scattering that removes planets from the system once the gas disk dissipates (e.g., Dong & Dawson 2016). Systems with two-arm spirals, however, are unlikely to have additional giant planets with similar masses at distances close enough to interact with the purported arm-driving planet, as such planets will drive their own sets of two-arm spirals, which are not seen.

Thus, the most attractive explanation for two-arm spirals in disks is that they are driven by massive giant planetary companions ($\gtrsim 5M_J$) that are fainter than predicted by hot start evolutionary models.

Planetary companions might also play a role in explaining multi-arm spirals. Numerical simulations have shown that a planet of mass $\sim M_J$ usually drives one to three arms on one side of its orbit that are detectable in NIR imaging observations (Dong & Fung 2017). In

disks with multi-arm spirals (Figure 1), the arms are at similar distances. To drive them with Jovian planets requires more than one planet, positioned over a small range of disk radii, potentially in conflict with theories of giant planet formation.

6. Summary and Future Prospects

Spiral arm structures are surprisingly common in NIR scattered light imaging of protoplanetary disks, especially among Herbig stars. Among the 11 Herbig stars that have been well-studied in scattered light, 6/11 have spiral arms of some kind, and 2/11 have near-symmetric two-arm spirals. Among the 24 single Herbig stars within 200 pc, 10 have been imaged in scattered light. The spiral arm occurrence rate in this volume-limited Herbig intermediate mass star (IMS) sample is $\geq 2/24$ for two-arm spirals and $\geq 5/24$ for spirals of all kinds; if some of the remaining 14 disks in the sample turn out to have spiral structures, the fractions will be higher. Although the sample studied to date is small and the occurrence rates of spiral arms poorly determined as a result, the data do have the potential to constrain quantities of fundamental importance for planet formation.

Two-arm spirals appear to be more common among Herbig IMS disks than are directly imaged giant planet companions to mature AB stars as estimated in the literature. This discrepancy is difficult to account for in a simple way given our current understanding of the mechanisms that can create spiral structure. Gravitational instability is unlikely to explain the two-arm spirals detected in class II disks mainly because of the short lifetime of this phase of disk evolution compared with the high fraction of two-arm spirals observed. The stellar accretion rates of Herbig systems with two-arm spirals are also not particularly high compared to other Herbig stars. To explain the high occurrence rate of two-arm spirals, we propose that they may be produced by massive giant planets that are fainter than predicted by hot start models. Such planets must occur as companions to $\gtrsim 8\%$ of Herbig IMS.

Gravitational instability may drive multi-arm spirals if the disk mass is $\gtrsim 10\%$ of the stellar mass. Submillimeter continuum-based disk mass estimates for disks with multi-arm spirals are generally about one order of magnitude below this threshold. However, the high stellar accretion rates of Herbig stars, if sustained over a reasonable fraction of their lifetimes, suggest much larger disk masses. As a result, gravitational instability is a plausible explanation for multi-arm spirals. With the multi-arm phase of gravitational instability persisting longer than the two-arm phase, it is possibly consistent with the 3/11 occurrence rate among well-studied Herbig IMS and the $\geq 3/24$ occurrence rate in the volume-limited Herbig IMS sample.

Several future studies can lend insights into the issues raised here. Our study is limited by the small sample size of disks that have been well-studied in scattered light. High signal-to-noise scattered light imaging of the remainder of the volume-limited Herbig IMS sample would be extremely valuable in firming up the occurrence rates of spiral features. ALMA observations of the gas and dust emission structure of disks, which do not require illumination by the central star, are a valuable way to develop a more complete census of spiral arms. To distinguish between the various scenarios that could produce the observed spiral structures, it may be useful to compare not only the observed and expected number and symmetry of arms but also the observed and expected surface brightness contrast of spiral features above the rest of the disk.

The current sample is biased toward older sources that lack substantial infall and are therefore less likely to have gravitationally unstable disks. It would be very interesting to search for spiral structure among the younger precursor population (i.e., among GK-type intermediate mass T Tauri stars) either in scattered light or millimeter emission. The time evolution of the occurrence rate of two-arm spirals may shed light on the formation timescale of giant planets at large distances, and those of multi-arm spirals may reveal how disk masses evolve with time.

Acknowledgments

We thank Jaehan Bae, Xuening Bai, Josh Eisner, Cassandra Hall, Jun Hashimoto, Scott Kenyon, Kaitlin Kratter, Adam Kraus and Ken Rice for valuable advice and discussions, and an anonymous referee for a helpful review of the manuscript. We are grateful to Henning Avenhaus, Myriam Benisty, Hector Canovas, Katherine Follette, Antonio Garufi, Jun Hashimoto, and Taichi Uyama for making available the observational images used in Figure 1. This research has made use of the SIMBAD database, operated at CDS, Strasbourg, France. SDB acknowledges NASA Agreements No. NXX15AD94G and No. NNX16AJ81G; and NSF-AST 1517014. JRN acknowledges the stimulating research environment supported by NASA Agreement No. NNX15AD94G to the “Earths in Other Solar Systems” program. SDB gratefully acknowledges the generous hospitality and stimulating scientific environment provided by the National Optical Astronomy Observatory.

REFERENCES

Akiyama, E., Muto, T., Kusakabe, N., et al. 2015, *ApJ*, 802, L17

- Akiyama, E., Hashimoto, J., Liu, H. B., et al. 2016, *AJ*, 152, 222
- Alcalá, J. M., Spezzi, L., Chapman, N., et al. 2008, *ApJ*, 676, 427
- ALMA Partnership, Brogan, C. L., Pérez, L. M., et al. 2015, *ApJ*, 808, L3
- Alonso-Albi, T., Fuente, A., Bachiller, R., et al. 2009, *A&A*, 497, 117
- Andrews, S. M., Rosenfeld, K. A., Kraus, A. L., & Wilner, D. J. 2013, *ApJ*, 771, 129
- Andrews, S. M., & Williams, J. P. 2005, *ApJ*, 631, 1134
- . 2007, *ApJ*, 671, 1800
- Andrews, S. M., Wilner, D. J., Espaillat, C., et al. 2011, *ApJ*, 732, 42
- Andrews, S. M., Wilner, D. J., Zhu, Z., et al. 2016, *ApJ*, 820, L40
- Antoniucci, S., Podio, L., Nisini, B., et al. 2016, *A&A*, 593, L13
- Augereau, J. C., Lagrange, A. M., Mouillet, D., & Ménard, F. 2001, *A&A*, 365, 78
- Avenhaus, H., Quanz, S. P., Schmid, H. M., et al. 2014, *ApJ*, 781, 87
- . 2017, *AJ*, 154, 33
- Avenhaus, H., Quanz, S. P., Garufi, A., et al. 2018, *ArXiv e-prints*, arXiv:1803.10882
- Bae, J., & Zhu, Z. 2018, *ApJ*, 859, 118
- Bae, J., Zhu, Z., & Hartmann, L. 2016, *ApJ*, 819, 134
- . 2017, *ApJ*, 850, 201
- Bai, X.-N. 2017, *ApJ*, 845, 75
- Bai, X.-N., Ye, J., Goodman, J., & Yuan, F. 2016, *ApJ*, 818, 152
- Balbus, S. A., & Hawley, J. F. 1992, *ApJ*, 400, 610
- Baraffe, I., Chabrier, G., Barman, T. S., Allard, F., & Hauschildt, P. H. 2003, *A&A*, 402, 701
- Beckwith, S. V. W., Sargent, A. I., Chini, R. S., & Guesten, R. 1990, *AJ*, 99, 924
- Benisty, M., Juhasz, A., Boccaletti, A., et al. 2015, *A&A*, 578, L6

- Benisty, M., Stolker, T., Pohl, A., et al. 2017, *A&A*, 597, A42
- Bergin, E. A., Cleeves, L. I., Gorti, U., et al. 2013, *Nature*, 493, 644
- Bertrang, G. H.-M., Avenhaus, H., Casassus, S., et al. 2018, *MNRAS*, 474, 5105
- Beskrovnaya, N. G., Pogodin, M. A., Miroshnichenko, A. S., et al. 1999, *A&A*, 343, 163
- Beuzit, J.-L., Feldt, M., Dohlen, K., et al. 2008, in *Society of Photo-Optical Instrumentation Engineers (SPIE) Conference Series*, Vol. 7014, *Society of Photo-Optical Instrumentation Engineers (SPIE) Conference Series*
- Biller, B. A., Liu, M. C., Rice, K., et al. 2015, *MNRAS*, 450, 4446
- Boccaletti, A., Pantin, E., Lagrange, A.-M., et al. 2013, *A&A*, 560, A20
- Boehler, Y., Weaver, E., Isella, A., et al. 2017, *ApJ*, 840, 60
- Bowler, B. P. 2016, *PASP*, 128, 102001
- Brittain, S. D., Simon, T., Najita, J. R., & Rettig, T. W. 2007, *ApJ*, 659, 685
- Brown, J. M., Rosenfeld, K. A., Andrews, S. M., Wilner, D. J., & van Dishoeck, E. F. 2012, *ApJ*, 758, L30
- Burrows, C. J., Stapelfeldt, K. R., Watson, A. M., et al. 1996, *ApJ*, 473, 437
- Canovas, H., Ménard, F., Hales, A., et al. 2013, *A&A*, 556, A123
- Canovas, H., Perez, S., Dougados, C., et al. 2015, *A&A*, 578, L1
- Canovas, H., Hardy, A., Zurlo, A., et al. 2017, *A&A*, 598, A43
- Canovas, H., Montesinos, B., Schreiber, M. R., et al. 2018, *A&A*, 610, A13
- Carpenter, J. M., Wolf, S., Schreyer, K., Launhardt, R., & Henning, T. 2005, *AJ*, 129, 1049
- Cauley, P. W., & Johns-Krull, C. M. 2014, *ApJ*, 797, 112
- Chabrier, G., Baraffe, I., Allard, F., & Hauschildt, P. 2000, *ApJ*, 542, 464
- Chen, C. H., Pecaut, M., Mamajek, E. E., Su, K. Y. L., & Bitner, M. 2012, *ApJ*, 756, 133
- Chun, M., Toomey, D., Wahhaj, Z., et al. 2008, in *Proc. SPIE*, Vol. 7015, *Adaptive Optics Systems*, 70151V

- Cieza, L. A., Casassus, S., Tobin, J., et al. 2016, *Nature*, 535, 258
- Cieza, L. A., Casassus, S., Pérez, S., et al. 2017, *ApJ*, 851, L23
- Clampin, M., Krist, J. E., Ardila, D. R., et al. 2003, *AJ*, 126, 385
- Cleeves, L. I., Öberg, K. I., Wilner, D. J., et al. 2016, *ApJ*, 832, 110
- Close, L. M., Roddier, F., Hora, J. L., et al. 1997, *ApJ*, 489, 210
- Cossins, P., Lodato, G., & Clarke, C. J. 2009, *MNRAS*, 393, 1157
- Cotera, A. S., Whitney, B. A., Young, E., et al. 2001, *ApJ*, 556, 958
- Cox, A. W., Grady, C. A., Hammel, H. B., et al. 2013, *ApJ*, 762, 40
- Currie, T., Cloutier, R., Brittain, S., et al. 2015, *ApJ*, 814, L27
- Currie, T., Muto, T., Kudo, T., et al. 2014, *ApJ*, 796, L30
- Currie, T., Grady, C. A., Cloutier, R., et al. 2016, *ApJ*, 819, L26
- Czekala, I., Andrews, S. M., Jensen, E. L. N., et al. 2015, *ApJ*, 806, 154
- D’Alessio, P., Cantö, J., Calvet, N., & Lizano, S. 1998, *ApJ*, 500, 411
- de Boer, J., Salter, G., Benisty, M., et al. 2016, *A&A*, 595, A114
- de Gregorio-Monsalvo, I., Ménard, F., Dent, W., et al. 2013, *A&A*, 557, A133
- de Leon, J., Takami, M., Karr, J. L., et al. 2015, *ApJ*, 806, L10
- Debes, J. H., Jang-Condell, H., Weinberger, A. J., Roberge, A., & Schneider, G. 2013, *ApJ*, 771, 45
- Debes, J. H., Poteet, C. A., Jang-Condell, H., et al. 2017, *ApJ*, 835, 205
- Dipierro, G., Price, D., Laibe, G., et al. 2015, *MNRAS*, 453, L73
- Dipierro, G., Ricci, L., Pérez, L., et al. 2018, *MNRAS*, 475, 5296
- Donehew, B., & Brittain, S. 2011, *AJ*, 141, 46
- Dong, R. 2015, *ApJ*, 810, 6
- Dong, R., & Dawson, R. 2016, *ApJ*, 825, 77

- Dong, R., & Fung, J. 2017, *ApJ*, 835, 38
- Dong, R., Fung, J., & Chiang, E. 2016a, *ApJ*, 826, 75
- Dong, R., Hall, C., Rice, K., & Chiang, E. 2015a, *ApJ*, 812, L32
- Dong, R., Li, S., Chiang, E., & Li, H. 2017a, *ApJ*, 843, 127
- Dong, R., Vorobyov, E., Pavlyuchenkov, Y., Chiang, E., & Liu, H. B. 2016b, *ApJ*, 823, 141
- Dong, R., Zhu, Z., Fung, J., et al. 2016c, *ApJ*, 816, L12
- Dong, R., Zhu, Z., Rafikov, R. R., & Stone, J. M. 2015b, *ApJ*, 809, L5
- Dong, R., Zhu, Z., & Whitney, B. 2015c, *ApJ*, 809, 93
- Dong, R., van der Marel, N., Hashimoto, J., et al. 2017b, *ApJ*, 836, 201
- Draine, B. T. 2006, *ApJ*, 636, 1114
- Ducati, J. R. 2002, *VizieR Online Data Catalog*, 2237
- Duchêne, G., McCabe, C., Ghez, A. M., & Macintosh, B. A. 2004, *ApJ*, 606, 969
- Dullemond, C. P., & Dominik, C. 2004, *A&A*, 417, 159
- Dunhill, A. C., Alexander, R. D., & Armitage, P. J. 2013, *MNRAS*, 428, 3072
- Dunkin, S. K., & Crawford, I. A. 1998, *MNRAS*, 298, 275
- Eisner, J. A., Bally, J. M., Ginsburg, A., & Sheehan, P. D. 2016, *ApJ*, 826, 16
- Eisner, J. A., Arce, H. G., Ballering, N. P., et al. 2018, *ApJ*, 860, 77
- Erickson, K. L., Wilking, B. A., Meyer, M. R., Robinson, J. G., & Stephenson, L. N. 2011, *AJ*, 142, 140
- Espaillet, C., Muzerolle, J., Najita, J., et al. 2014, *Protostars and Planets VI*, 497
- Evans, M. G., Ilee, J. D., Hartquist, T. W., et al. 2017, *MNRAS*, 470, 1828
- Facchini, S., Birnstiel, T., Bruderer, S., & van Dishoeck, E. F. 2017, *A&A*, 605, A16
- Fairlamb, J. R., Oudmaijer, R. D., Mendigutía, I., Ilee, J. D., & van den Ancker, M. E. 2015, *MNRAS*, 453, 976

- Fairlamb, J. R., Oudmaijer, R. D., Mendigutia, I., Ilee, J. D., & van den Ancker, M. E. 2017, MNRAS, 464, 4721
- Fedele, D., Carney, M., Hogerheijde, M. R., et al. 2017, A&A, 600, A72
- Fedele, D., Tazzari, M., Booth, R., et al. 2018, A&A, 610, A24
- Finkenzeller, U., & Mundt, R. 1984, A&AS, 55, 109
- Flaherty, K. M., Hughes, A. M., Andrews, S. M., et al. 2016, ApJ, 818, 97
- Follette, K. B., Tamura, M., Hashimoto, J., et al. 2013, ApJ, 767, 10
- Follette, K. B., Grady, C. A., Swearingen, J. R., et al. 2015, ApJ, 798, 132
- Follette, K. B., Rameau, J., Dong, R., et al. 2017, AJ, 153, 264
- Folsom, C. P., Bagnulo, S., Wade, G. A., et al. 2012, MNRAS, 422, 2072
- Forgan, D., & Rice, K. 2013, MNRAS, 433, 1796
- Fortney, J. J., Marley, M. S., Saumon, D., & Lodders, K. 2008, ApJ, 683, 1104
- Fossati, L., Ryabchikova, T., Bagnulo, S., et al. 2009, A&A, 503, 945
- Fukagawa, M., Tamura, M., Itoh, Y., Hayashi, S. S., & Oasa, Y. 2003, ApJ, 590, L49
- Fukagawa, M., Tamura, M., Itoh, Y., et al. 2006, ApJ, 636, L153
- Fukagawa, M., Hayashi, M., Tamura, M., et al. 2004, ApJ, 605, L53
- Fung, J., & Dong, R. 2015, ApJ, 815, L21
- Gaia Collaboration, Brown, A. G. A., Vallenari, A., et al. 2016, A&A, 595, A2
- Gammie, C. F. 2001, ApJ, 553, 174
- Garcia Lopez, R., Natta, A., Testi, L., & Habart, E. 2006, A&A, 459, 837
- Garufi, A., Quanz, S. P., Schmid, H. M., et al. 2014, A&A, 568, A40
- Garufi, A., Quanz, S. P., Avenhaus, H., et al. 2013, A&A, 560, A105
- Garufi, A., Quanz, S. P., Schmid, H. M., et al. 2016, A&A, 588, A8
- Garufi, A., Meeus, G., Benisty, M., et al. 2017, A&A, 603, A21

- Ginski, C., Stolker, T., Pinilla, P., et al. 2016, *A&A*, 595, A112
- Goldreich, P., & Lynden-Bell, D. 1965, *MNRAS*, 130, 97
- Goldreich, P., & Tremaine, S. 1979, *ApJ*, 233, 857
- Grady, C. A., Polomski, E. F., Henning, T., et al. 2001, *AJ*, 122, 3396
- Grady, C. A., Schneider, G., Hamaguchi, K., et al. 2007, *ApJ*, 665, 1391
- Grady, C. A., Schneider, G., Sitko, M. L., et al. 2009, *ApJ*, 699, 1822
- Grady, C. A., Hamaguchi, K., Schneider, G., et al. 2010, *ApJ*, 719, 1565
- Grady, C. A., Muto, T., Hashimoto, J., et al. 2013, *ApJ*, 762, 48
- Greene, T. P., & Meyer, M. R. 1995, *ApJ*, 450, 233
- Guimarães, M. M., Alencar, S. H. P., Corradi, W. J. B., & Vieira, S. L. A. 2006, *A&A*, 457, 581
- Hall, C., Forgan, D., Rice, K., et al. 2016, *MNRAS*, 458, 306
- Hamidouche, M. 2010, *ApJ*, 722, 204
- Hartmann, L., Calvet, N., Gullbring, E., & D’Alessio, P. 1998, *ApJ*, 495, 385
- Hashimoto, J., Tamura, M., Muto, T., et al. 2011, *ApJ*, 729, L17
- Hashimoto, J., Dong, R., Kudo, T., et al. 2012, *ApJ*, 758, L19
- Hashimoto, J., Tsukagoshi, T., Brown, J. M., et al. 2015, *ApJ*, 799, 43
- Hayashi, C. 1981, *Progress of Theoretical Physics Supplement*, 70, 35
- Henning, T., Launhardt, R., Steinacker, J., & Thamm, E. 1994, *A&A*, 291, 546
- Hernández, J., Calvet, N., Briceño, C., Hartmann, L., & Berlind, P. 2004, *AJ*, 127, 1682
- Hernández, J., Calvet, N., Hartmann, L., et al. 2005, *AJ*, 129, 856
- Hernández, J., Hartmann, L., Calvet, N., et al. 2008, *ApJ*, 686, 1195
- Høg, E., Fabricius, C., Makarov, V. V., et al. 2000, *A&A*, 355, L27
- Honda, M., Inoue, A. K., Fukagawa, M., et al. 2009, *ApJ*, 690, L110

- Houk, N., & Cowley, A. P. 1975, University of Michigan Catalogue of two-dimensional spectral types for the HD stars. Volume I. Declinations -90 to -53 degree
- Huang, J., Andrews, S. M., Cleeves, L. I., et al. 2018, *ApJ*, 852, 122
- Isella, A., Carpenter, J. M., & Sargent, A. I. 2009, *ApJ*, 701, 260
- Isella, A., & Turner, N. J. 2018, *ApJ*, 860, 27
- Isella, A., Guidi, G., Testi, L., et al. 2016, *Physical Review Letters*, 117, 251101
- Itoh, Y., Tamura, M., Hayashi, S. S., et al. 2002, *PASJ*, 54, 963
- Itoh, Y., Oasa, Y., Kudo, T., et al. 2014, *Research in Astronomy and Astrophysics*, 14, 1438
- Jamialahmadi, N., Berio, P., Meilland, A., et al. 2015, *A&A*, 579, A81
- Janson, M., Thalmann, C., Boccaletti, A., et al. 2016, *ApJ*, 816, L1
- Jayawardhana, R., Luhman, K. L., D'Alessio, P., & Stauffer, J. R. 2002, *ApJ*, 571, L51
- Juhász, A., Benisty, M., Pohl, A., et al. 2015, *MNRAS*, 451, 1147
- Kama, M., Folsom, C. P., & Pinilla, P. 2015, *A&A*, 582, L10
- Kasper, M., Santhakumari, K. K. R., Herbst, T. M., & Köhler, R. 2016, *A&A*, 593, A50
- Kley, W., & Nelson, R. P. 2012, *ARA&A*, 50, 211
- Konishi, M., Grady, C. A., Schneider, G., et al. 2016, *ApJ*, 818, L23
- Kooistra, R., Kamp, I., Fukagawa, M., et al. 2017, *A&A*, 597, A132
- Kratter, K., & Lodato, G. 2016, *ARA&A*, 54, 271
- Kratter, K. M., Matzner, C. D., & Krumholz, M. R. 2008, *ApJ*, 681, 375
- Kratter, K. M., Matzner, C. D., Krumholz, M. R., & Klein, R. I. 2010, *ApJ*, 708, 1585
- Kraus, S., Ireland, M. J., Sitko, M. L., et al. 2013, *ApJ*, 768, 80
- Kraus, S., Kreplin, A., Fukugawa, M., et al. 2017, *ApJ*, 848, L11
- Krist, J. E., Stapelfeldt, K. R., Ménard, F., Padgett, D. L., & Burrows, C. J. 2000, *ApJ*, 538, 793
- Krist, J. E., Stapelfeldt, K. R., & Watson, A. M. 2002, *ApJ*, 570, 785

- Krist, J. E., Stapelfeldt, K. R., Golimowski, D. A., et al. 2005, *AJ*, 130, 2778
- Kudo, T., Tamura, M., Kitamura, Y., et al. 2008, *ApJ*, 673, L67
- Kusakabe, N., Grady, C. A., Sitko, M. L., et al. 2012, *ApJ*, 753, 153
- Lacour, S., Biller, B., Cheetham, A., et al. 2016, *A&A*, 590, A90
- Langlois, M., Pohl, A., Lagrange, A.-M., et al. 2018, *A&A*, 614, A88
- Lee, W.-K. 2016, *ApJ*, 832, 166
- Lenzen, R., Hartung, M., Brandner, W., et al. 2003, in *Proc. SPIE, Vol. 4841, Instrument Design and Performance for Optical/Infrared Ground-based Telescopes*, ed. M. Iye & A. F. M. Moorwood, 944–952
- Ligi, R., Vigan, A., Gratton, R., et al. 2018, *MNRAS*, 473, 1774
- Liu, H. B., Galván-Madrid, R., Vorobyov, E. I., et al. 2016a, *ApJ*, 816, L29
- Liu, H. B., Takami, M., Kudo, T., et al. 2016b, *Science Advances*, 2, e1500875
- Lodato, G., & Rice, W. K. M. 2004, *MNRAS*, 351, 630
- . 2005, *MNRAS*, 358, 1489
- Long, Z. C., Fernandes, R. B., Sitko, M., et al. 2017, *ApJ*, 838, 62
- Loomis, R. A., Öberg, K. I., Andrews, S. M., & MacGregor, M. A. 2017, *ApJ*, 840, 23
- Lucas, P. W., Fukagawa, M., Tamura, M., et al. 2004, *MNRAS*, 352, 1347
- Macintosh, B. A., Graham, J. R., Palmer, D. W., et al. 2008, in *Society of Photo-Optical Instrumentation Engineers (SPIE) Conference Series, Vol. 7015, Society of Photo-Optical Instrumentation Engineers (SPIE) Conference Series*
- Maire, A.-L., Stolker, T., Messina, S., et al. 2017, *A&A*, 601, A134
- Malfait, K., Bogaert, E., & Waelkens, C. 1998, *A&A*, 331, 211
- Mandy, M. E., & Martin, P. G. 1993, *ApJS*, 86, 199
- Manoj, P., Bhatt, H. C., Maheswar, G., & Muneer, S. 2006, *ApJ*, 653, 657
- Mathis, J. S. 1990, *ARA&A*, 28, 37

- Mathis, J. S., Rumpl, W., & Nordsieck, K. H. 1977, *ApJ*, 217, 425
- Mawet, D., Choquet, É., Absil, O., et al. 2017, *AJ*, 153, 44
- Mayama, S., Hashimoto, J., Muto, T., et al. 2012, *ApJ*, 760, L26
- McCabe, C., Duchêne, G., & Ghez, A. M. 2002, *ApJ*, 575, 974
- McClure, M. K., Bergin, E. A., Cleves, L. I., et al. 2016, *ApJ*, 831, 167
- Mendigutía, I., Oudmaiher, R. D., Mourard, D., & Muzerolle, J. 2017a, *MNRAS*, 464, 1984
- Mendigutía, I., Oudmaiher, R. D., Garufi, A., et al. 2017b, *A&A*, 608, A104
- Meru, F., Juhász, A., Ilee, J. D., et al. 2017, *ApJ*, 839, L24
- Momose, M., Ohashi, N., Kudo, T., Tamura, M., & Kitamura, Y. 2010, *ApJ*, 712, 397
- Momose, M., Morita, A., Fukagawa, M., et al. 2015, *PASJ*, 67, 83
- Monnier, J. D., Harries, T. J., Aarnio, A., et al. 2017, *ApJ*, 838, 20
- Montesinos, M., Perez, S., Casassus, S., et al. 2016, *ApJ*, 823, L8
- Morzinski, K. M., Close, L. M., Males, J. R., et al. 2014, in *Proc. SPIE*, Vol. 9148, *Adaptive Optics Systems IV*, 914804
- Mouillet, D., Lagrange, A. M., Augereau, J. C., & Ménard, F. 2001, *A&A*, 372, L61
- Muñoz, D. J., & Lai, D. 2016, *ApJ*, 827, 43
- Murakawa, K., Oya, S., Pyo, T.-S., & Ishii, M. 2008, *A&A*, 492, 731
- Murphy, S. J., & Paunzen, E. 2017, *MNRAS*, 466, 546
- Muto, T., Grady, C. A., Hashimoto, J., et al. 2012, *ApJ*, 748, L22
- Muzerolle, J., D’Alessio, P., Calvet, N., & Hartmann, L. 2004, *ApJ*, 617, 406
- Najita, J. R., & Kenyon, S. J. 2014, *MNRAS*, 445, 3315
- Öberg, K. I., Guzmán, V. V., Furuya, K., et al. 2015, *Nature*, 520, 198
- Ogilvie, G. I., & Lubow, S. H. 2002, *MNRAS*, 330, 950
- Oh, D., Hashimoto, J., Tamura, M., et al. 2016a, *PASJ*, 68, L3

- Oh, D., Hashimoto, J., Carson, J. C., et al. 2016b, *ApJ*, 831, L7
- Ohta, Y., Fukagawa, M., Sitko, M. L., et al. 2016, *PASJ*, 68, 53
- Pascucci, I., Testi, L., Herczeg, G. J., et al. 2016, *ApJ*, 831, 125
- Pecaut, M. J., & Mamajek, E. E. 2013, *ApJS*, 208, 9
- Pérez, L. M., Carpenter, J. M., Andrews, S. M., et al. 2016, *Science*, 353, 1519
- Perrin, M. D., Duchêne, G., Kalas, P., & Graham, J. R. 2006, *ApJ*, 645, 1272
- Perrin, M. D., Schneider, G., Duchene, G., et al. 2009, *ApJ*, 707, L132
- Perrot, C., Boccaletti, A., Pantin, E., et al. 2016, *A&A*, 590, L7
- Pfalzner, S. 2003, *ApJ*, 592, 986
- Pinilla, P., Birnstiel, T., Ricci, L., et al. 2012, *A&A*, 538, A114
- Pinilla, P., de Boer, J., Benisty, M., et al. 2015, *A&A*, 584, L4
- Pinte, C., Padgett, D. L., Ménard, F., et al. 2008, *A&A*, 489, 633
- Pohl, A., Sissa, E., Langlois, M., et al. 2017a, *A&A*, 605, A34
- Pohl, A., Benisty, M., Pinilla, P., et al. 2017b, *ApJ*, 850, 52
- Price, D. J., Cuello, N., Pinte, C., et al. 2018, *MNRAS*, 477, 1270
- Quanz, S. P., Avenhaus, H., Buenzli, E., et al. 2013, *ApJ*, 766, L2
- Quanz, S. P., Birkmann, S. M., Apai, D., Wolf, S., & Henning, T. 2012, *A&A*, 538, A92
- Quanz, S. P., Schmid, H. M., Geissler, K., et al. 2011, *ApJ*, 738, 23
- Rameau, J., Chauvin, G., Lagrange, A.-M., et al. 2012, *A&A*, 546, A24
- Rameau, J., Follette, K. B., Pueyo, L., et al. 2017, *AJ*, 153, 244
- Rapson, V. A., Kastner, J. H., Andrews, S. M., et al. 2015a, *ApJ*, 803, L10
- Rapson, V. A., Kastner, J. H., Millar-Blanchaer, M. A., & Dong, R. 2015b, *ApJ*, 815, L26
- Reggiani, M., Christiaens, V., Absil, O., et al. 2018, *A&A*, 611, A74
- Ren, B., Dong, R., Esposito, T. M., et al. 2018, *ApJ*, 857, L9

- Rice, W. K. M., & Armitage, P. J. 2009, MNRAS, 396, 2228
- Rice, W. K. M., Armitage, P. J., Bate, M. R., & Bonnell, I. A. 2003, MNRAS, 339, 1025
- Rich, E. A., Wisniewski, J. P., Mayama, S., et al. 2015, AJ, 150, 86
- Richert, A. J. W., Getman, K. V., Feigelson, E. D., et al. 2018, MNRAS, 477, 5191
- Rodgers, B. M. 2001, PhD thesis, UNIVERSITY OF WASHINGTON
- Rodigas, T. J., Follette, K. B., Weinberger, A., Close, L., & Hines, D. C. 2014, ApJ, 791, L37
- Rosenfeld, K. A., Andrews, S. M., Wilner, D. J., Kastner, J. H., & McClure, M. K. 2013, ApJ, 775, 136
- Rosotti, G. P., Clarke, C. J., Manara, C. F., & Facchini, S. 2017, MNRAS, 468, 1631
- Sandell, G., Weintraub, D. A., & Hamidouche, M. 2011, ApJ, 727, 26
- Sartori, M. J., Gregorio-Hetem, J., Rodrigues, C. V., Hetem, Jr., A., & Batalha, C. 2010, AJ, 139, 27
- Schneider, G., Grady, C. A., Hines, D. C., et al. 2014, AJ, 148, 59
- Sicilia-Aguilar, A., Henning, T., & Hartmann, L. W. 2010, ApJ, 710, 597
- Siess, L., Dufour, E., & Forestini, M. 2000, A&A, 358, 593
- Silber, J., Gledhill, T., Duchêne, G., & Ménard, F. 2000, ApJ, 536, L89
- Spezzi, L., Alcalá, J. M., Covino, E., et al. 2008, ApJ, 680, 1295
- Spiegel, D. S., & Burrows, A. 2012, ApJ, 745, 174
- Stamatellos, D., & Whitworth, A. P. 2008, A&A, 480, 879
- Stapelfeldt, K. R., Krist, J. E., Ménard, F., et al. 1998, ApJ, 502, L65
- Stapelfeldt, K. R., Ménard, F., Watson, A. M., et al. 2003, ApJ, 589, 410
- Stapelfeldt, K. R., Watson, A. M., Krist, J. E., et al. 1999, ApJ, 516, L95
- Stolker, T., Dominik, C., Avenhaus, H., et al. 2016, A&A, 595, A113
- Stolker, T., Sitko, M., Lazareff, B., et al. 2017, ApJ, 849, 143

- Takami, M., Karr, J. L., Hashimoto, J., et al. 2013, *ApJ*, 772, 145
- Tamura, M. 2009, in *American Institute of Physics Conference Series*, Vol. 1158, American Institute of Physics Conference Series, ed. T. Usuda, M. Tamura, & M. Ishii, 11–16
- Tamura, M., Suto, H., Itoh, Y., et al. 2000, in *Proc. SPIE*, Vol. 4008, *Optical and IR Telescope Instrumentation and Detectors*, ed. M. Iye & A. F. Moorwood, 1153–1161
- Tamura, M., Hodapp, K., Takami, H., et al. 2006, in *Proc. SPIE*, Vol. 6269, *Society of Photo-Optical Instrumentation Engineers (SPIE) Conference Series*, 62690V
- Tang, Y.-W., Guilloteau, S., Piétu, V., et al. 2012, *A&A*, 547, A84
- Tang, Y.-W., Guilloteau, S., Dutrey, A., et al. 2017, *ApJ*, 840, 32
- Tanii, R., Itoh, Y., Kudo, T., et al. 2012, *PASJ*, 64, 124
- Thalmann, C., Grady, C. A., Goto, M., et al. 2010, *ApJ*, 718, L87
- Thalmann, C., Mulders, G. D., Hodapp, K., et al. 2014, *A&A*, 566, A51
- Thalmann, C., Mulders, G. D., Janson, M., et al. 2015, *ApJ*, 808, L41
- Thalmann, C., Janson, M., Garufi, A., et al. 2016, *ApJ*, 828, L17
- The, P. S., de Winter, D., & Perez, M. R. 1994, *A&AS*, 104, 315
- Thi, W. F., Ménard, F., Meeus, G., et al. 2013, *A&A*, 557, A111
- Tobin, J. J., Kratter, K. M., Persson, M. V., et al. 2016, *Nature*, 538, 483
- Tomida, K., Machida, M. N., Hosokawa, T., Sakurai, Y., & Lin, C. H. 2017, *ApJ*, 835, L11
- Toomre, A. 1964, *ApJ*, 139, 1217
- Tsukagoshi, T., Momose, M., Hashimoto, J., et al. 2014, *ApJ*, 783, 90
- Uyama, T., Hashimoto, J., Kuzuhara, M., et al. 2017, *AJ*, 153, 106
- Uyama, T., Hashimoto, J., Muto, T., et al. 2018, *ArXiv e-prints*, arXiv:1804.05934
- Valdes, F., Gupta, R., Rose, J. A., Singh, H. P., & Bell, D. J. 2004, *ApJS*, 152, 251
- Valenti, J. A., Fallon, A. A., & Johns-Krull, C. M. 2003, *ApJS*, 147, 305
- van Boekel, R., Henning, T., Menu, J., et al. 2017, *ApJ*, 837, 132

- van den Ancker, M. E., The, P. S., & de Winter, D. 1996, *A&A*, 309, 809
- van der Marel, N., Verhaar, B. W., van Terwisga, S., et al. 2016, *A&A*, 592, A126
- van der Marel, N., van Dishoeck, E. F., Bruderer, S., et al. 2013, *Science*, 340, 1199
- Vieira, S. L. A., Corradi, W. J. B., Alencar, S. H. P., et al. 2003, *AJ*, 126, 2971
- Vigan, A., Bonavita, M., Biller, B., et al. 2017, *A&A*, 603, A3
- Vorobyov, E. I., & Basu, S. 2005, *ApJ*, 633, L137
- . 2010, *ApJ*, 719, 1896
- Wagner, K., Apai, D., Kasper, M., & Robberto, M. 2015, *ApJ*, 813, L2
- Wagner, K., Dong, R., Sheehan, P., et al. 2018, *ApJ*, 854, 130
- Wahhaj, Z., Cieza, L. A., Mawet, D., et al. 2015, *A&A*, 581, A24
- Walker, H. J., & Wolstencroft, R. D. 1988, *PASP*, 100, 1509
- Walsh, C., Juhász, A., Meeus, G., et al. 2016, *ApJ*, 831, 200
- Walsh, C., Juhász, A., Pinilla, P., et al. 2014, *ApJ*, 791, L6
- Watson, A. M., & Stapelfeldt, K. R. 2004, *ApJ*, 602, 860
- Weinberger, A. J., Becklin, E. E., Schneider, G., et al. 1999, *ApJ*, 525, L53
- . 2002, *ApJ*, 566, 409
- White, J. A., Boley, A. C., Hughes, A. M., et al. 2016, *ApJ*, 829, 6
- Williams, J. P., & Best, W. M. J. 2014, *ApJ*, 788, 59
- Wolff, S. G., Perrin, M., Millar-Blanchaer, M. A., et al. 2016, *ApJ*, 818, L15
- Yang, Y., Hashimoto, J., Hayashi, S. S., et al. 2017, *AJ*, 153, 7
- Zacharias, N., Finch, C. T., Girard, T. M., et al. 2012, *VizieR Online Data Catalog*, 1322
- Zhang, K., Isella, A., Carpenter, J. M., & Blake, G. A. 2014, *ApJ*, 791, 42
- Zhu, Z., Dong, R., Stone, J. M., & Rafikov, R. R. 2015, *ApJ*, 813, 88
- Zhu, Z., Nelson, R. P., Dong, R., Espaillat, C., & Hartmann, L. 2012, *ApJ*, 755, 6

#	Object	Spiral	L_\star	T_{eff}	SpT	D	M_\star	f_{mm}	λ_{mm}	R_{mm}	M_{dust}	M_{disk}/M_\star
(1)	(2)	(3)	L_\odot	K	(6)	pc	M_\odot	mJy	μm	AU	M_\oplus	$\times 1\%$
3	AB Aur	Multiple	43.8 ¹	9380	B9.5 ¹¹	153 ¹⁶	2.50	309 ¹	890	230 ³⁰	50	0.6
4	MWC 480	None	19.6 ¹	8330	A5	142 ¹⁶	2.04	331 ¹⁷	1167	170	95	1.4
6	MWC 758	$m \approx 2$	8.5 ²	7600	A8 ¹²	151 ¹⁶	1.68	180 ²	880	151	36	0.7
...	V1247 Ori	One Arm	15.8 ³	7880	F0 ¹³	320 ¹⁶	1.91	300 ¹⁸	870	190	252	4.0
10	HD 97048	None	36.1 ³	10500	A0	179 ¹⁶	2.50	2230 ¹⁹	867	403	737	8.8
13	HD 100546	Multiple	24.7 ³	9750	B9 ¹⁴	109 ¹⁶	2.30	1240 ²⁰	867	230	118	1.5
17	SAO 206462	$m \approx 2$	8.8 ³	6375	F4	156 ¹⁶	1.70	620 ²	880	156	136	2.4
21	HD 142527	Multiple	9.9 ³	6500	F6	156 ¹⁶	1.70	3310 ²¹	880	300	1126	19.9
26	IRS 48	None	20.4 ⁴	9530	A0	120	2.25	180 ⁶	850	60 ³¹	10	0.1
33	HD 163296	None	23.6 ³	9250	A2 ¹¹	119 ¹⁶	2.18	1820 ²²	850	250	210	2.9
34	HD 169142	None	6.1 ⁵	6700	F3	117 ¹⁶	1.51	232 ²³	1288	100	60	1.2
...	LkHa 330	$m \approx 2$	12.8 ⁶	5830	G3	250	2.12	210 ²	880	170	110	1.6
...	FN Tau	None	0.5 ⁷	3240	M5	140	0.30	37 ²⁴	882	...	19	1.9
...	RY Tau	None	23.1 ¹	5080	K1	177 ¹⁶	3.30	469 ¹	890	200 ³²	116	1.1
...	UX Tau	None	2.0 ¹	4900	G8	158 ¹⁶	1.60	150 ²	880	85	37	0.7
...	LkCa 15	None	1.0 ⁶	4730	K5	140	1.27	410 ²	880	182	191	4.5
...	GM Aur	None	1.2 ¹	4730	K3	140	1.16	640 ²	880	120	193	5.0
...	SU Aur	None	10.7 ¹	5520	G8	142 ¹⁶	2.25	71 ¹	890	...	12	0.2
...	TW Hya	None	0.4 ⁶	4210	M2	60 ¹⁶	1.00	1500 ²⁵	867	65	75	2.2
...	DZ Cha	$m \approx 2$	0.6 ⁸	3770	M0	110	0.51	74 ⁸	517	...	6	0.4
...	PDS 66	None	1.4 ⁶	5080	K1	99 ¹⁶	1.30	207 ²⁶	1200	...	73	1.7
...	PDS 70	None	1.2 ⁹	4140	K5 ¹⁵	140	0.83	38 ²⁷	1300	100	26	0.9
...	IM Lupi	None	0.9 ¹⁰	3900	M0	161 ¹⁶	0.60	590 ¹⁰	875	300	614	30.7
...	J1604-2130	None	0.6 ⁶	4350	K2	145	1.10	226 ²	880	145 ³³	116	3.2
...	Sz 91	None	0.3 ⁶	3720	M0.5	200	0.48	42 ²⁸	860	160	60	3.7
...	RX J1615.3-3255	None	1.3 ²	4350	K5	185	1.10	430 ²	880	185	317	8.6
...	DoAr 28	None	0.7 ⁶	4370	K5	139	1.12	69 ²⁹	1300	...	77	2.1
...	SR 21	None	6.5 ⁶	5830	G3	120	1.67	400 ²	880	84	38	0.7
...	V4046 Sgr	None	0.7 ⁶	4350	K5	73	1.10	770 ⁶	850	73 ³⁴	49	1.3

Table 1: Stellar and disk properties for the “well-studied NIR disks” sample (§2.1). Column (1): Source number from Table 2. Column (2): Source name; RA and Dec available in Appendix Table E.2. Column (3): Type of spiral. Column (4): Stellar luminosity (rescaled by Gaia Collaboration et al. (2016) distance if available). Column (5): Effective temperature; references omitted if the same as in Col. (4). Column (6): Spectral type; references omitted if the same as in Col. (4). Column (7): Distance; references omitted if the same as in Col. (4). Distances from Gaia Collaboration et al. (2016) unless otherwise noted. Column (8): Stellar mass from Siess et al. (2000) tracks, using listed T_{eff} and L_\star . Column (9): Flux density of millimeter continuum emission. Column (10): The wavelength at which Col. (8) is measured. Column (11): Disk radius in millimeter continuum emission; references omitted if the same as in Col. (8). Column (12): Dust mass derived from the submillimeter flux; see Appendix §B for details. Column (13): Disk mass (M_{disk}) in units of the stellar mass, where M_{disk} is $100\times$ the dust mass in Col. (11). References can be found at the end of Table 2.

#	Object	Spiral	Included?	SpT	L_\star L_\odot	T_{eff} K	D pc	M_\star M_\odot	R_\star R_\odot	f_{mm} mJy	λ_{mm} μm	R_{mm} AU	M_{dust} M_\oplus	$\log L_{\text{acc}}$ L_\odot , Lit.	$\log L_{\text{Br}\gamma}$ L_\odot , Lit.	$\log L_{\text{H}\alpha}$ L_\odot , Lit.	$\log L_{\text{acc}}$ L_\odot	$\log \dot{M}_\star$ (19)
(1)	(2)	(3)	(4)	(5)	(6)	(7)	(8)	(9)	(10)	(11)	(12)	(13)	(14)	(15)	(16)	(17)	(18)	(19)
1	HR811	...	No	B7 ³⁵	87.1 ⁴⁰	14000	120 ¹⁶	4.00	3.00	-1.49	0.60 ⁵²	-7.02
2	V892 Tau	...	No	A0 ¹⁴	39.8 ⁴¹	11220	160	2.75	2.02	630 ⁴³	850	100 ⁵³	62	-1.44	0.65 ⁵⁴	-6.98
3	AB Aur	Multiple	Yes	B9.5 ¹¹	43.8 ¹	9380	153 ¹⁶	2.50	2.53	309 ¹	890	230	50	...	-2.68	...	1.08 ⁵⁵	-6.41
4	MWC 480	None	Yes	A5 ¹	19.6 ¹	8330	142 ¹⁶	2.04	2.09	331 ¹⁷	1167	170	95	...	-3.00	...	0.65 ⁵⁵	-6.84
5	PDS 178	...	No	A2/A7 ³⁶	23.4 ⁴²	8910	150	2.20	1.96	20 ⁴⁴	1200	...	7	-1.78	0.31 ⁵⁶	-7.23
6	MWC 758	$m \approx 2$	Yes	A8 ³⁷	8.5 ²	7600	151 ¹⁶	1.68	1.68	180 ²	880	151	36	...	-3.15	...	0.45 ⁵⁵	-7.05
7	CQ Tau	...	No	F5 ⁹	10.7 ⁴¹	6760	160 ¹⁶	1.71	2.35	143 ⁴⁴	1300	...	90	...	-4.08	...	-0.61 ⁵⁵	-7.97
8	PDS201	...	Yes	A7 ³⁷	9.5 ⁴⁰	7850	168 ¹⁶	1.76	1.76	-1.95	0.14 ⁵⁷	-7.36
9	HD56895	...	Yes	F0 ³⁵	11.7 ⁴⁰	7500	167 ¹⁶	1.80	1.92
10	HD 97048	None	Yes	A0 ¹⁴	36.2 ³	10500	179 ¹⁶	2.50	1.85	2230 ¹⁹	867	403	736	...	-2.81	...	0.86 ⁵⁸	-6.77
11	HIP 54557	...	Yes	B9 ³⁵	20.9 ⁴⁰	10700	184 ¹⁶	2.61	1.95	-3.35	...	0.11 ⁵⁹	-7.51
12	HD 100453	...	No	A9 ³⁸	6.0 ³	7250	103 ¹⁶	1.54	1.79	182 ⁴⁶	1300	...	58	-2.35	-0.26 ⁵⁸	-7.69
13	HD 100546	Multiple	Yes	B9 ³⁷	24.7 ³	9750	109 ¹⁶	2.30	2.58	1240 ²⁰	867	230	118	0.56	0.66 ³	-6.78
14	HD104237	...	Yes	A0 ¹⁴	20.9 ³	8000	104 ¹⁶	1.97	2.28	66 ⁴⁵	1300	...	14	0.7	0.61 ³	-6.82
15	PDS 141	...	Yes	F0 ³⁹	19.0 ³⁹	7200	180	1.92	2.73	1470 ⁴⁷	1200	...	796	-1.15	0.94 ³⁹	-6.40
16	PDS389	...	Yes	A3 ³⁷	8.9 ³⁷	8710	175	1.96	1.87	-1.84	0.25 ⁶⁰	-7.27
17	SAO 206462	$m \approx 2$	Yes	F4 ¹⁴	8.8 ³	6375	156 ¹⁶	1.70	2.54	620 ²	880	156	136	-0.04	0.05 ³	-7.27
18	PDS 395	...	Yes	A8 ³⁷	5.8 ³	7750	131 ¹⁶	1.74	1.71	242 ⁴⁴	1300	...	129	-0.1	-0.16 ³	-7.66
19	HD141569	...	No	A0 ³⁷	18.8 ³	9750	111 ¹⁶	2.26	2.58	13 ⁴⁸	870	60	1	-0.05	-0.06 ³	-7.50
20	PDS 76	...	Yes	A8 ³⁷	9.8 ³	7500	150 ¹⁶	1.78	1.78	313 ⁴³	850	...	65	...	-3.63	...	-0.22 ⁵⁸	-7.72
21	HD 142527	Multiple	Yes	F6 ³⁵	9.9 ³	6500	156 ¹⁶	1.70	2.52	3310 ²¹	880	300	1126	-0.09	0.01 ³	-7.32
22	PDS 78	...	Yes	A8 ³⁷	11.0 ³	7500	160 ¹⁶	1.80	1.93	37 ⁴⁴	1300	...	23	0.02	0.02 ³	-7.44
23	HR 5999	...	No	A7 ¹⁴	59.6 ³	8500	163 ¹⁶	2.53	3.09	60 ⁴³	850	...	8	1.1	1.12 ³	-6.29
24	PDS 80	...	Yes	A8 ³⁷	8.2 ³	8000	149 ¹⁶	1.76	1.75	-2.34	-0.25 ⁵⁸	-7.75
25	HIP80425	...	Yes	A1 ³⁸	15.9 ⁴⁰	9200	152 ¹⁶	2.39	2.17
26	IRS 48	None	Yes	A0 ⁴	20.4 ⁴	9530	120	2.25	2.52	1000 ⁴⁹	441	60	12	...	-3.35	...	0.11 ⁴	-7.34
27	WLY 1-53	...	Yes	A7 ⁴	17.4 ⁴	7850	130	1.91	2.13	-3.67	...	-0.32 ⁶¹	-7.76
28	HD148352	...	Yes	F2 ⁴	16.2 ⁴	6890	130	1.90	2.70
29	HIP81474	...	Yes	B9.5 ³⁵	78.1 ⁴⁰	10400	149 ¹⁶	2.73	2.78	-3.04	...	0.50 ⁵⁹	-6.98
30	MWC863	...	No	B9.5 ³⁵	23.8 ³	9000	145	2.20	1.94	101 ⁴³	850	...	14	0.1	0.27 ³	-7.28
31	AK Sco	...	No	F5 ¹⁵	4.7 ³	6250	143 ¹⁶	1.43	1.72	33 ⁵⁰	1300	140	18	...	-2.60	...	1.45 ⁵⁸	-5.96
32	51 Oph	...	No	A2 ³⁵	147.9 ⁴⁰	9700	124 ¹⁶	3.20	3.75	5 ⁵¹	1200	...	1	...	-1.99	...	1.87 ⁵⁹	-5.56
33	HD 163296	None	Yes	A2 ¹¹	23.4 ³	9250	119 ¹⁶	2.18	1.84	1820 ²²	850	250	210	0.08	0.22 ³	-7.35
34	HD 169142	None	Yes	F3 ⁵	6.0 ⁵	6700	117 ¹⁶	1.51	1.90	232 ²³	1288	100	60	...	-3.08	...	0.45 ⁵⁹	-6.95
35	TY CrA	...	No	B9 ¹⁴	37.2 ⁴⁰	10700	130	2.61	1.95	-3.78	...	-0.46 ⁶²	-8.08
36	T CrA	...	No	F0 ¹⁴	1.6 ⁴⁰	7200	130	1.54	1.78	-3.94	...	-0.66 ⁶²	-8.09

Table 2 continued from previous page

#	Object	Spiral	Included?	SpT	L_\star L_\odot	T_{eff} K	D pc	M_\star M_\odot	R_\star R_\odot	f_{mm} mJy	λ_{mm} μm	R_{mm} AU	M_{dust} M_\oplus	$\log L_{\text{acc}}$ L_\odot , Lit.	$\log L_{\text{Br}\gamma}$ L_\odot , Lit.	$\log L_{\text{H}\alpha}$ L_\odot , Lit.	$\log L_{\text{acc}}$ L_\odot	$\log \dot{M}_\star$ (19)
(1)	(2)	(3)	(4)	(5)	(6)	(7)	(8)	(9)	(10)	(11)	(12)	(13)	(14)	(15)	(16)	(17)	(18)	(19)

Table 2: The sample of Herbig IMS within 200 pc introduced in §2.3. Note that this list includes objects that are not studied in this paper, such as multiples. Column (1): Source number, ordered by RA. Column (2): Source name; RA and Dec available in Appendix Table E.2; notes on individual stars can be found in Appendix §D. Column (3): Type of Spiral; omitted if high sensitivity high resolution scattered light imaging unavailable. Column (4): Whether the source is included in our “volume-limited Herbig IMS” sample (§2.3). Column (5): Spectral Type. Column (6): Stellar luminosity, rescaled by Gaia distance if available. Column (7): Effective temperature; references omitted if the same as in Col. (6). Column (8): Distance; references omitted if the same as in Col. (6); distances from Gaia Collaboration et al. (2016) adopted if available. Column (9): Stellar mass. Column (10): Stellar radius. Cols. (9) and (10) are derived from Siess et al. (2000) tracks and the listed T_{eff} and L_\star . Column (11): Flux density of millimeter continuum emission. Column (12): Wavelength at which Col. (10) is measured. Column (13): Disk radius in $\sim\text{mm}$ continuum emission; references omitted if the same as Col. (10). Column (14): Dust mass from Eqn. (B1); see Appendix §B for details. Column (15): Accretion luminosity from veiling of the Balmer discontinuity; references listed in Col. (17). Column (16): $\text{Br}\gamma$ emission line flux from literature; references listed in Col. (17). Column (17): $\text{H}\alpha$ emission line flux from literature; references listed in Col. (17). Column (18): Accretion luminosity adopted in this work; see Appendix §C for details. Column (19): Stellar accretion rate from Eqn. (C4) and Cols. (8), (9), and (17).

References in Tables 1 and 2. ¹ ² ³ ⁴ ⁵ ⁶ ⁷ ⁸ ⁹ ¹⁰ ¹¹ ¹² ¹³ ¹⁴ ¹⁵ ¹⁶ ¹⁷ ¹⁸ ¹⁹ ²⁰ ²¹ ²² ²³

¹Andrews et al. (2013)

²Andrews et al. (2011)

³Fairlamb et al. (2015)

⁴Erickson et al. (2011)

⁵Murphy & Paunzen (2017)

⁶van der Marel et al. (2016)

⁷Kudo et al. (2008)

⁸Canovas et al. (2018)

⁹Stellar temperature estimated from the spectral type using Pecaut & Mamajek (2013); luminosity calculated from the photometry reported in SIMBAD.

¹⁰Cleeves et al. (2016)

¹¹Valenti et al. (2003)

¹²Beskrovnaya et al. (1999)

¹³Kraus et al. (2013)

¹⁴The et al. (1994)

¹⁵SIMBAD

¹⁶Gaia Collaboration et al. (2016)

¹⁷Öberg et al. (2015)

¹⁸Kraus et al. (2017)

¹⁹Walsh et al. (2016)

²⁰Walsh et al. (2014)

²¹Boehler et al. (2017)

²²de Gregorio-Monsalvo et al. (2013)

²³Fedele et al. (2017)

²⁴Momose et al. (2010)

²⁵Andrews et al. (2016)

²⁶Carpenter et al. (2005)

²⁷Hashimoto et al. (2015)

²⁸Zhang et al. (2014)

²⁹Rich et al. (2015)

³⁰Tang et al. (2012)

³¹Brown et al. (2012)

³²Isella et al. (2009)

³³Dong et al. (2017b)

³⁴Rosenfeld et al. (2013)

³⁵Malfait et al. (1998)

³⁶Walker & Wolstencroft (1988)

³⁷Vieira et al. (2003)

³⁸Chen et al. (2012)

³⁹Spezzi et al. (2008)

⁴⁰This work; see Appendix D for details.

⁴¹Hernández et al. (2005)

⁴²Manoj et al. (2006)

⁴³Sandell et al. (2011)

⁴⁴Alonso-Albi et al. (2009)

⁴⁵Henning et al. (1994)

⁴⁶Menard et al. in prep.

⁴⁷Alcalá et al. (2008)

⁴⁸White et al. (2016)

⁴⁹van der Marel et al. (2013)

⁵⁰Czekala et al. (2015)

⁵¹Thi et al. (2013)

⁵²Valdes et al. (2004)

⁵³Hamidouche (2010)

57 58 59 60 61 62

⁵⁴Hernández et al. (2004)

⁵⁵Donehew & Brittain (2011)

⁵⁶Dunkin & Crawford (1998)

⁵⁷van den Ancker et al. (1996)

⁵⁸Fairlamb et al. (2017)

⁵⁹Garcia Lopez et al. (2006)

⁶⁰Sartori et al. (2010)

⁶¹Greene & Meyer (1995)

⁶²Finkenzeller & Mundt (1984)

Table 3. Incidence Rate of Spiral Arms in the “Well-Studied NIR Disks” Sample

	All Stars	AB Stars	FGK Stars	Herbig IMS
Two arms	4/29	1/7	3/22	2/11
Multiple arms	3/29	2/7	1/22	3/11
One arm	1/29		1/22	1/11
All arm types	8/29	3/7	5/22	6/11

Table 4. Incidence Rate of Spiral Arms in the “Volume-limited Herbig IMS” Sample

	All Types of Arms	Two Arms	Multiple Arms
Sources with arms	5	2	3
Arm fraction, well-studied disks	5/10	2/10	3/10
Arm fraction, all disks	$\geq 5/24$	$\geq 2/24$	$\geq 3/24$

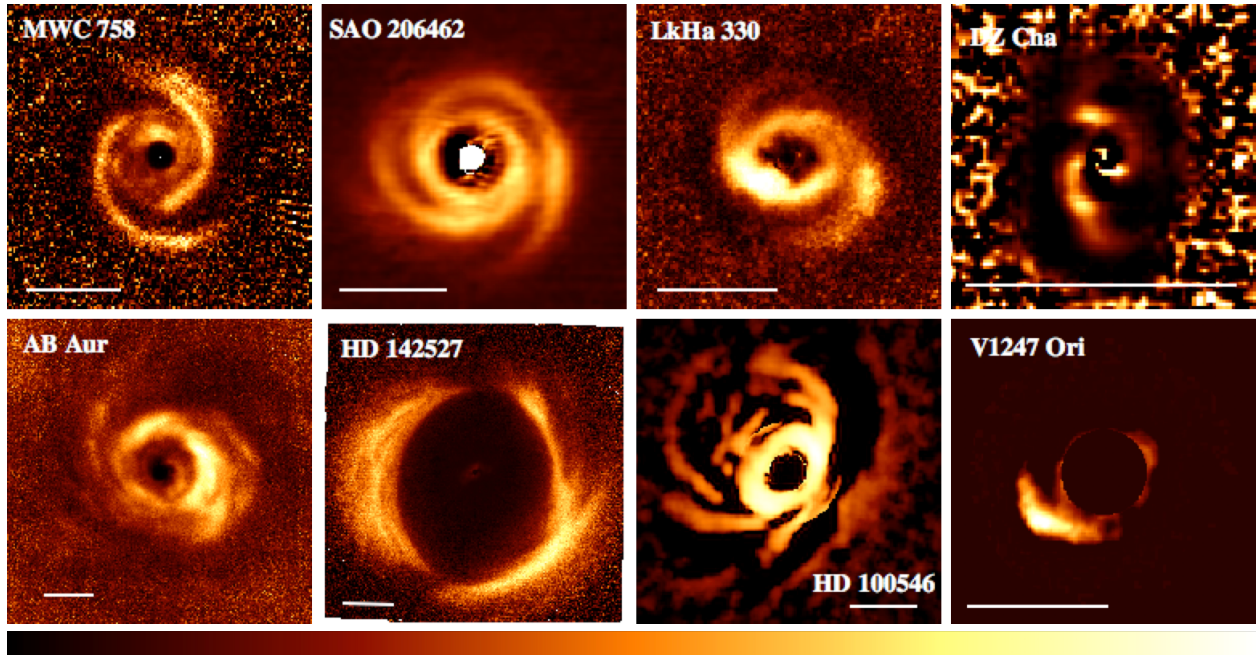


Fig. 1.— NIR scattered light images of disks with spiral arms. A set of prominent two-arm spirals are detected in MWC 758 (Benisty et al. 2015), SAO 206462 (Garufi et al. 2013), LkH α 330 (Uyama et al. 2018), and DZ Cha (Canovas et al. 2018). Multiple weak arms are observed on smaller scales in AB Aur (Hashimoto et al. 2011), HD 142527 (Avenhaus et al. 2017), and HD 100546 (Follette et al. 2017). A one-arm spiral is observed in V1247 Ori (Ohta et al. 2016). The scale bar in all panels is $0''.5$. All images show polarized intensity, and are r^2 -scaled and on a linear stretch, except for HD 100546, which shows total intensity and is on a log stretch because the polarized intensity image does not reveal the spiral arms well (Follette et al. 2017).

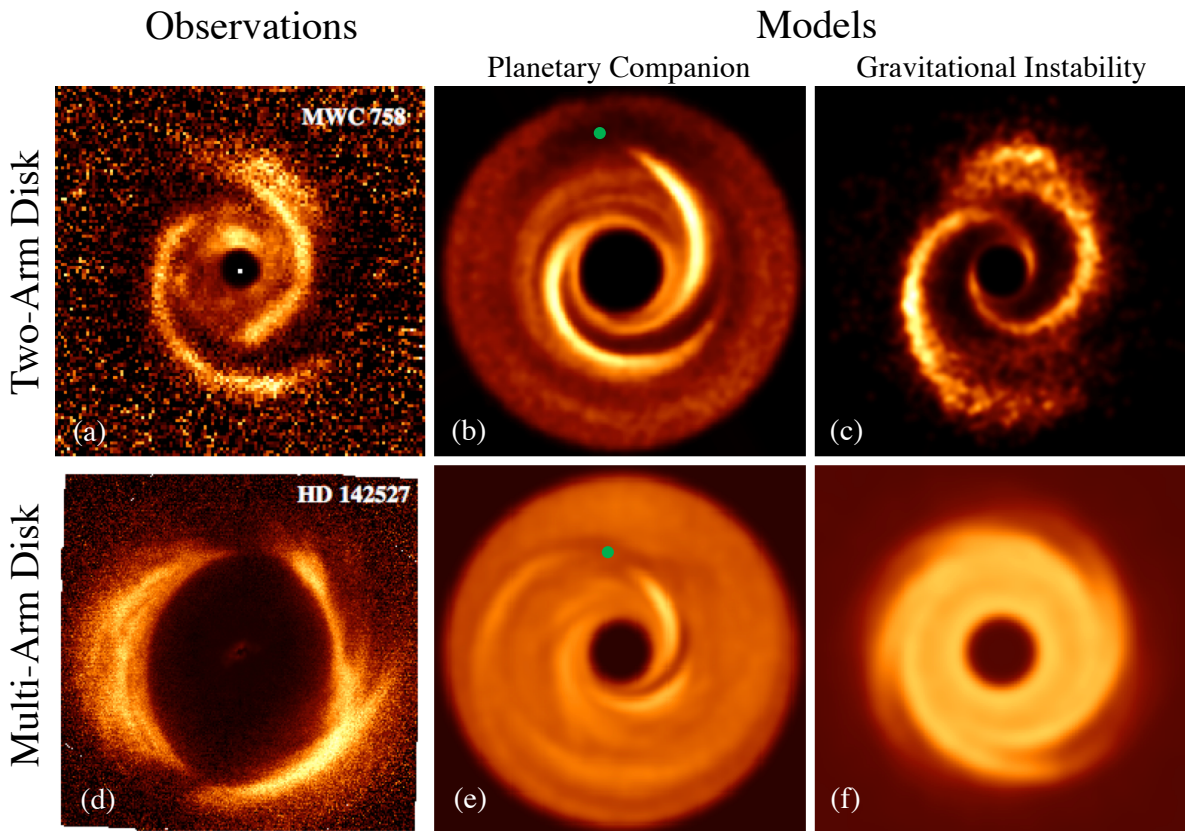


Fig. 2.— Examples of observed and modeled spiral structure in disks. Observed two-arm and multi-arm spirals (left column, Panels a and d) are compared with images from simulations of spiral arms created by orbiting companions (center column) with $M_p/M_\star = 0.006$ (Dong et al. 2015b, green dot; Panel b) and $M_p/M_\star = 0.001$ (Dong & Fung 2017, green dot; Panel e) and gravitationally unstable disks (right column) with $M_{\text{disk}}/M_\star = 0.5$ (Dong et al. 2015a, Panel c) and $M_{\text{disk}}/M_\star = 0.1$ (Dong et al. 2015a, Panel f). All images have been scaled by r^2 to enhance the faint outer disk, and the color stretch is linear in arbitrary units.

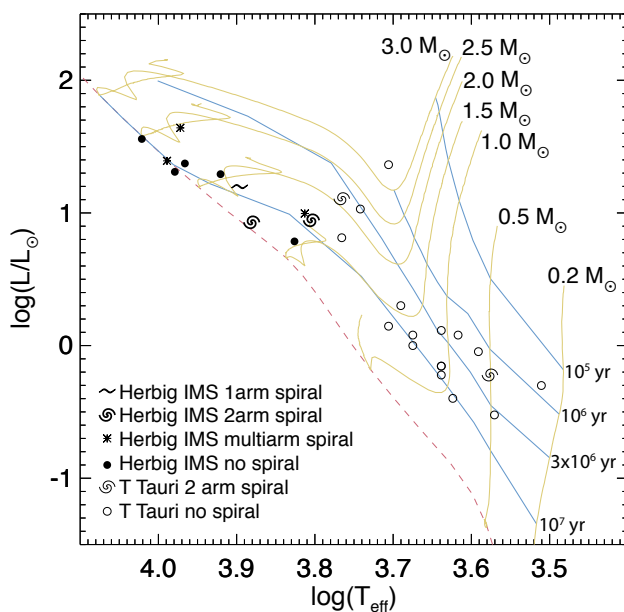


Fig. 3.— HR diagram for young stars with disks that have been well-studied in scattered light. Disks with multi-arm spirals (asterisks), two-arm spirals (spiral symbol), one-arm spirals (twiddle symbol), and no arms (circles and dots) are shown for Herbig IMS (heavy symbols, dots) and T Tauri stars (light symbols, open circles). Evolutionary tracks and isochrones from Siess et al. (2000) are also shown.

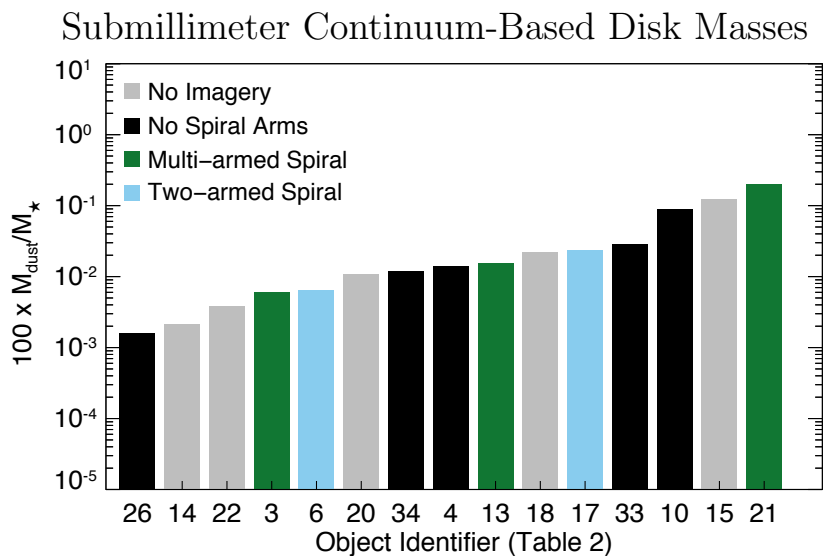


Fig. 4.— Ratio of $M_{\text{disk}}/M_{\star}$ for the volume-limited Herbig IMS sample (§2.3). The disk mass is estimated from the submillimeter continuum, assuming a gas-to-dust mass ratio of 100. The source name corresponding to each number in the horizontal axis can be found in Table 2. All disk masses are $< 0.2M_{\star}$, with the average $M_{\text{disk}}/M_{\star} = 0.008$. Herbig stars with spiral structure are interspersed with other Herbig stars. See §4 for details.

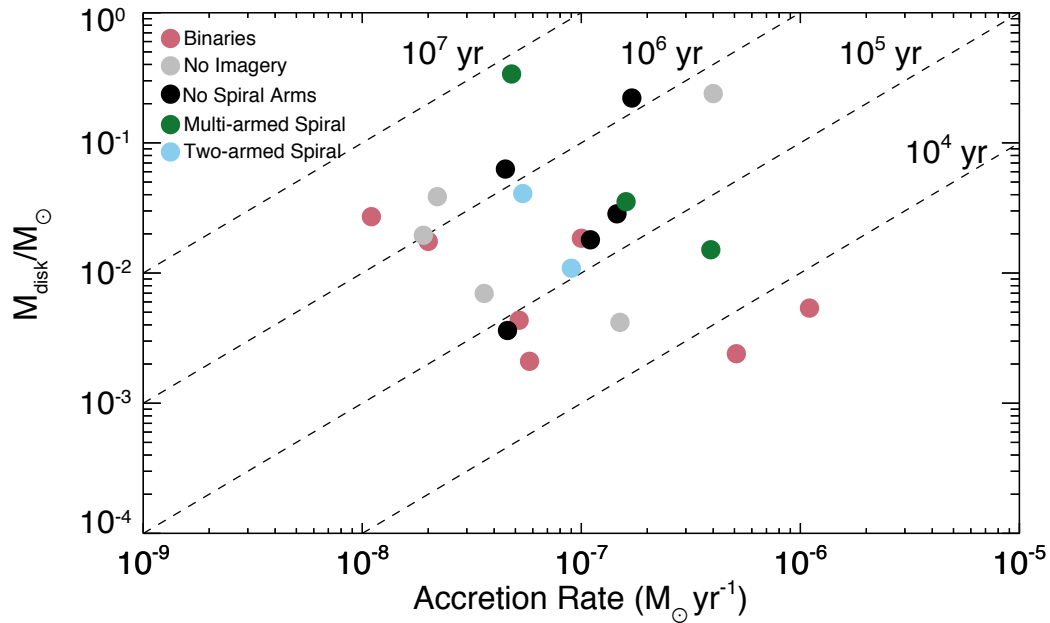


Fig. 5.— Submillimeter continuum-based disk mass (M_{disk}) plotted against stellar accretion rate (\dot{M}_*) for the volume-limited Herbig IMS sample. Diagonal dashed lines are lines of constant remaining disk lifetime ($\tau_{\text{life}} = M_{\text{disk}}/\dot{M}_*$). Over half of the sample is consistent with a disk lifetime of $\lesssim 2 \times 10^5$ years. See §4 and §5 for details.

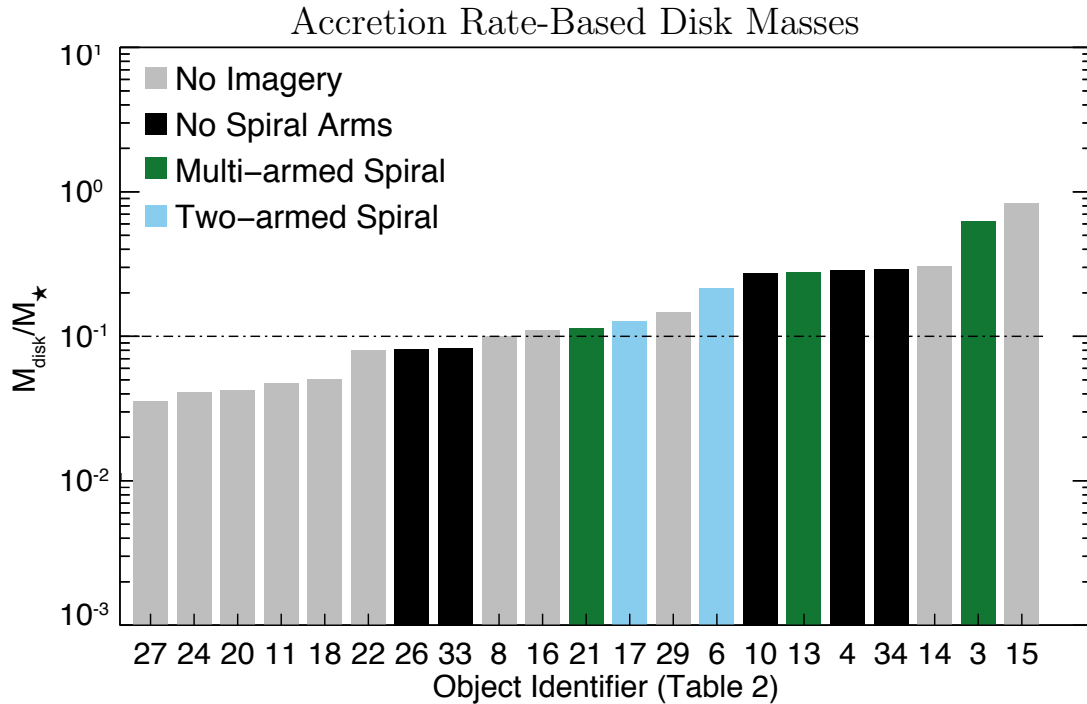


Fig. 6.— The ratio $M_{\text{disk}}/M_{\star}$ for the volume-limited Herbig IMS sample, where the disk mass is estimated as $2\dot{M}_{\star}t_0$ ($t_0=2$ Myr). Approximately one-half of the sources have $M_{\text{disk}} \gtrsim 0.1M_{\star}$. Herbig with spiral structure have $M_{\text{disk}}/M_{\star}$ as large as ~ 1 and in the upper half of the distribution, suggesting that disk mass may play a role in generating some of the spiral structures. See §4 and §5 for details.

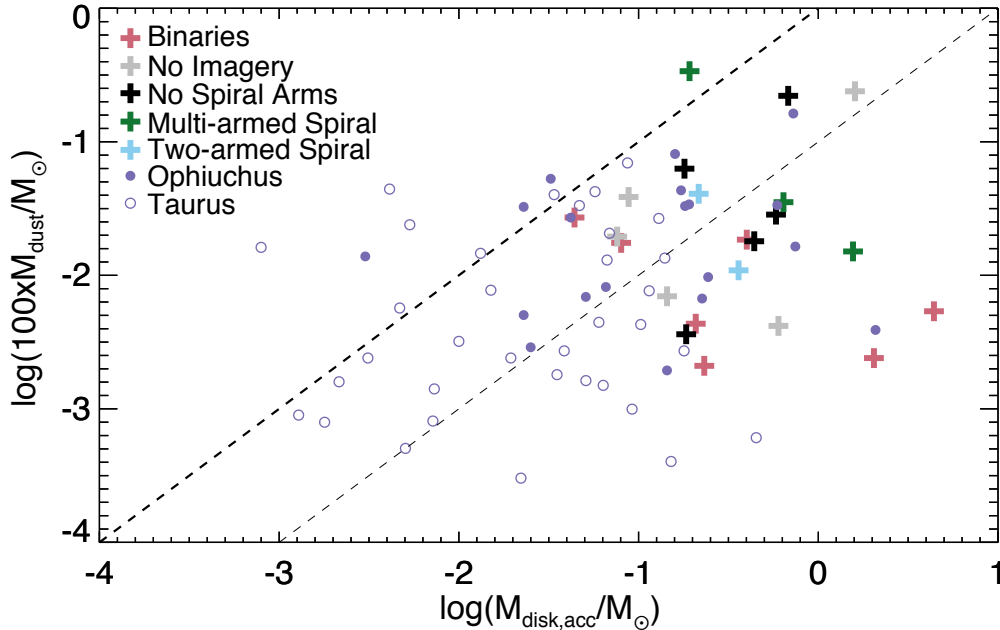


Fig. 7.— Disk masses estimated from submillimeter dust continuum emission (vertical axis) and from stellar accretion rates (horizontal axis). The thick (thin) dashed lines demarcate continuum-based disk masses that are equal to (one-tenth of) accretion rate-based disk masses. For both the Herbig IMS studied here (colored pluses) and T Tauri stars studied by Andrews & Williams (2007, Taurus—open circles; Ophiuchus—closed circles), stellar accretion rate-based disk masses are a few to tens of times larger than continuum-based disk masses. The average ratio of the disk mass inferred from the stellar accretion rate and the disk mass inferred from the flux of the submillimeter continuum is 8.1 ± 0.4 . See §4 and §5 for details.

A. Scattered Light Disk Sample

Table A.1. Scattered Light Protoplanetary Disk Sample

Target (1)	Instrument (2)	Wavelength (3)	Intensity (4)	Mode (5)	Reference (6)
AA Tau	HST / STIS	optical	total	Coro	Cox et al. (2013)
AB Aur	Subaru / CIAO	H	total	Coro	Fukagawa et al. (2004)
...	HST / NICMOS	$1.1\mu\text{m}, 2\mu\text{m}$	pol, total	Coro	Perrin et al. (2009)
...	Subaru / HiCIAO	H	pol	Coro	Hashimoto et al. (2011)
AK Sco	VLT / SPHERE	Y, J, H	total	Coro	Janson et al. (2016)
DoAr 28	Subaru / HiCIAO	H	pol	DI	Rich et al. (2015)
DZ Cha	VLT / SPHERE	J	pol	DI+Coro	Canovas et al. (2018)
FN Tau	Subaru / CIAO	H	total	Coro	Kudo et al. (2008)
GG Tau	HST / NICMOS	$1\mu\text{m}$	pol	DI	Silber et al. (2000)
...	HST / WFPC2	optical	total	DI	Krist et al. (2002)
...	HST / NICMOS	1.1 to $2\mu\text{m}$	total	DI	McCabe et al. (2002)
...	Subaru / CIAO	H	total	Coro	Itoh et al. (2002)
...	Keck / NIRC2	L'	total	DI	Duchêne et al. (2004)
...	HST / ACS	optical	total	DI	Krist et al. (2005)
...	Subaru / HiCIAO	H	pol	Coro	Itoh et al. (2014)
...	Subaru / HiCIAO	H	pol	DI	Yang et al. (2017)
GM Aur	Subaru / HiCIAO	H	pol	DI	Oh et al. (2016b)
HD 100453	VLT / SPHERE	Y, J, H, K	total	DI	Wagner et al. (2015)
...	VLT / SPHERE	optical, J	pol	DI+Coro	Benisty et al. (2017)
...	Gemini / GPI	Y, J, K_1	pol	DI	Long et al. (2017)
HD 100546	HST / STIS	1.1 to $2\mu\text{m}$	total	Coro	Grady et al. (2001)
...	HST / NICMOS2	H	total	Coro	Augereau et al. (2001)
...	VLT / NACO	H, K_s	pol	DI	Quanz et al. (2011)
...	Gemini / NICI	K_s	total	Coro	Boccaletti et al. (2013)
...	VLT / NACO	H, K_s, L'	pol	DI	Avenhaus et al. (2014)
...	Gemini / NICI	K_s, L'	total	DI	Currie et al. (2014)
...	Gemini / GPI	H	pol, total	DI+Coro	Currie et al. (2015)
...	VLT / SPHERE	optical, H, K	pol, total	DI+Coro	Garufi et al. (2016)
...	Gemini / GPI, Magellan / MagAO	optical, H	total	DI+Coro	Rameau et al. (2017)
...	Gemini / GPI, Magellan / MagAO	optical, Y, H	pol, total	Coro	Follette et al. (2017)
HD 141569	HST / NICMOS	$1.1\mu\text{m}$	total	Coro	Weinberger et al. (1999)
...	HST / STIS	optical	total	Coro	Mouillet et al. (2001)
...	HST / ACS	optical	total	Coro	Clampin et al. (2003)
...	Gemini / NICI	H	total	Coro	Billler et al. (2015)
...	HST / STIS	optical	total	Coro	Konishi et al. (2016)
...	Keck / NIRC2	L'	total	DI	Currie et al. (2016)
...	VLT / SPHERE	Y, J, H, K	total	Coro	Perrot et al. (2016)
HD 142527	Subaru / CIAO	H, K	total	Coro	Fukagawa et al. (2006)
...	Subaru / CIAO	$3\mu\text{m}, L'$	total	DI+Coro	Honda et al. (2009)
...	VLT / NACO	L'	total	DI	Rameau et al. (2012)
...	VLT / NACO	H, K_s	pol	DI	Canovas et al. (2013)
...	Gemini / GPI	Y	pol	DI	Rodigas et al. (2014)
...	VLT / NACO	H, K_s	pol	DI	Avenhaus et al. (2014)
...	VLT / SPHERE	optical	pol	DI	Mendigutía et al. (2017b)
...	VLT / SPHERE	optical	pol	DI	Avenhaus et al. (2017)

Table A.1—Continued

Target (1)	Instrument (2)	Wavelength (3)	Intensity (4)	Mode (5)	Reference (6)
HD 150193	Subaru / CIAO	H	total	Coro	Fukagawa et al. (2003)
HD 163296	VLT / NACO	H, K_s	pol	DI	Garufi et al. (2014)
...	Gemini / GPI	J	pol	Coro	Monnier et al. (2017)
...	VLT / NACO	K_s	pol	DI	Garufi et al. (2017)
HD 169142	HST / NICMOS	$1.1 \mu\text{m}$	total	Coro	Grady et al. (2007)
...	VLT / NACO	H	pol	DI	Quanz et al. (2013)
...	Subaru / HiCIAO	H	pol	Coro	Momose et al. (2015)
...	VLT / SPHERE	optical, Y, J, H	pol	Coro	Pohl et al. (2017b)
...	Gemini / GPI	J	pol	Coro	Monnier et al. (2017)
...	VLT / SPHERE	Y, J, H, K	pol, total	DI+Coro	Ligi et al. (2018)
...	VLT / SPHERE	optical	pol	DI	Bertrang et al. (2018)
HD 97048	VLT / NACO	H, K_s	pol	DI	Quanz et al. (2012)
...	VLT / SPHERE	J, H	pol, total	Coro	Ginski et al. (2016)
IM Lupi	HST / WFPC2 / NICMOS	optical, H	total	DI+Coro	Pinte et al. (2008)
IRS 48	Subaru / HiCIAO	H, K_s	pol	DI	Follette et al. (2015)
J1604-2130	Subaru / HiCIAO	H	pol	DI	Mayama et al. (2012)
...	VLT / SPHERE	optical	pol	DI	Pinilla et al. (2015)
...	VLT / SPHERE	Y, J, H, K	total	Coro	Canovas et al. (2017)
LkCa 15	Subaru / HiCIAO	H, K_s	total	DI	Thalmann et al. (2010)
...	Gemini / NIRI	K_s	total	DI	Thalmann et al. (2014)
...	VLT / SPHERE	optical	pol	DI	Thalmann et al. (2015)
...	Subaru / HiCIAO	H	pol	DI	Oh et al. (2016a)
...	VLT / SPHERE	J	pol	DI+Coro	Thalmann et al. (2016)
LkH α 330	Subaru / HiCIAO	H	pol	DI	Akiyama et al. (2016)
...	Subaru / HiCIAO	H, K	pol	DI	Uyama et al. (2018)
MWC 480	HST / NICMOS	$1.1, 1.6 \mu\text{m}$	total	Coro	Grady et al. (2010)
...	Subaru / HiCIAO	H	pol	Coro	Kusakabe et al. (2012)
MWC 758	Subaru / CIAO	H	pol	DI+Coro	Grady et al. (2013)
...	VLT / SPHERE	Y	pol	Coro	Benisty et al. (2015)
...	Keck / NIRC2	L'	total	Coro	Reggiani et al. (2018)
...	Keck / NIRC2	L'	total	Coro	Ren et al. (2018)
PDS 66	HST / STIS	$1.1 \mu\text{m}$	total	Coro	Schneider et al. (2014)
...	Gemini / GPI	H, K_1	pol	Coro	Wolff et al. (2016)
PDS 70	Subaru / HiCIAO	H	pol	DI	Hashimoto et al. (2012)
RX J1615.3-3255	Subaru / HiCIAO	H	pol	DI	Kooistra et al. (2017)
...	VLT / SPHERE	optical, Y, J, H	pol, total	DI+Coro	de Boer et al. (2016)
RY Lup	VLT / SPHERE	Y, J, H	pol, total	DI+Coro	Langlois et al. (2018)
RY Tau	Subaru / HiCIAO	H	pol	Coro	Takami et al. (2013)
SAO 206462	HST / NICMOS	optical, $1.1 \mu\text{m}, 1.6 \mu\text{m}$	total	DI+Coro	Grady et al. (2009)
...	Subaru / HiCIAO	H	pol	DI	Muto et al. (2012)
...	VLT / NACO	H, K_s	pol	DI	Garufi et al. (2013)
...	Gemini / GPI	J	total	Coro	Wahhaj et al. (2015)
...	VLT / SPHERE	optical, Y, J	pol	DI+Coro	Stolker et al. (2016)
...	VLT / SPHERE	J, H, K	pol	Coro	Stolker et al. (2017)
...	VLT / SPHERE	Y, J, H, K	total	Coro	Maire et al. (2017)

Table A.1—Continued

Target (1)	Instrument (2)	Wavelength (3)	Intensity (4)	Mode (5)	Reference (6)
SR 21	Subaru / HiCIAO	H	pol	DI	Follette et al. (2013)
SU Aur	Subaru / HiCIAO	H	pol	DI	de Leon et al. (2015)
Sz 91	Subaru / HiCIAO	K_s	pol	DI	Tsukagoshi et al. (2014)
T Cha	VLT / SPHERE	optical, Y, J, H	pol, total	Coro	Pohl et al. (2017a)
T Tau	VLT / SPHERE	J, H	total	Coro	Kasper et al. (2016)
TW Hya	HST / WFPC2	optical	total	DI	Krist et al. (2000)
...	HST / NICMOS	1.1 μ m, 1.6 μ m	total	Coro	Weinberger et al. (2002)
...	HST / STIS	optical, 1.1-2.2 μ m	total	Coro	Debes et al. (2013)
...	Subaru / HiCIAO	H	pol	DI	Akiyama et al. (2015)
...	Gemini / GPI	J, K_1	pol	Coro	Rapson et al. (2015b)
...	VLT / SPHERE	optical, J, H	pol	DI+Coro	van Boekel et al. (2017)
...	HST / STIS	optical	total	Coro	Debes et al. (2017)
UX Tau	Subaru / HiCIAO	H	pol	Coro	Tanii et al. (2012)
V1247 Ori	Subaru / HiCIAO	H	pol	Coro	Ohta et al. (2016)
V4046 Sgr	Gemini / GPI	J, K_2	pol	Coro	Rapson et al. (2015a)
Edge On Sources (Central Source Invisible)					
HH 30	HST / WFPC2	optical	total	DI	Burrows et al. (1996)
...	HST / WFPC2	optical	total	DI	Stapelfeldt et al. (1999)
...	HST / NICMOS	1-2 μ m	total	DI	Cotera et al. (2001)
...	HST / WFPC2	optical	total	DI	Watson & Stapelfeldt (2004)
HK Tau	HST / WFPC2	optical	total	DI	Stapelfeldt et al. (1998)
HV Tau C	HST / WFPC2	optical	total	DI	Stapelfeldt et al. (2003)
LkH α 263C	Gemini / Hokupa	H	total	DI	Jayawardhana et al. (2002)
PDS 144 N	Keck / NIRC2	H, K, L'	total	DI	Perrin et al. (2006)
Partially Embedded / Class 0 / Class I Sources					
FU Ori	Subaru / HiCIAO	H	pol	Coro	Liu et al. (2016a)
HL Tau	Subaru / CIAO	J, H, K	pol	DI	Lucas et al. (2004)
...	Subaru / CIAO	J, H, K	pol	DI	Murakawa et al. (2008)
R Mon	HST / WFPC2	J, H, K	pol, total	DI	Close et al. (1997)
V1057 Cyg	Subaru / HiCIAO	H	pol	Coro	Liu et al. (2016a)
V1735 Cyg	Subaru / HiCIAO	H	pol	Coro	Liu et al. (2016a)
Z CMa	VLT / SPHERE	H, K	pol	DI	Canovas et al. (2015)
...	VLT / SPHERE	optical	total	DI	Antonucci et al. (2016)
...	Subaru / HiCIAO	H	pol	Coro	Liu et al. (2016a)

Note. — Column (2): the instrument used in each observation, including STIS, NICMOS, ACS, and WFPC2 on HST, CIAO (Tamura et al. 2000) and HiCIAO (Tamura et al. 2006) on Subaru, NICI (Chun et al. 2008) and GPI (Macintosh et al. 2008) on Gemini, NACO (Lenzen et al. 2003) and SPHERE (Beuzit et al. 2008) on VLT, NIRC2 on Keck, and MagAO on Magellan (Morzinski et al. 2014). Column (4): “pol” – polarized intensity; “total” – total intensity. Column (5): observing mode; “Coro” – coronagraphic imaging; “DI” – direct imaging with no coronagraph. See §2 for details.

B. Disk Mass Measurements

The direct measurement of the mass of an accretion disk around a young star is almost impossible. Most of the disk mass is comprised of molecular hydrogen which lacks a dipole moment and whose lowest energy emission line has an upper state energy level of 510 K (Mandy & Martin 1993). Thus emission lines from this molecule only trace relatively warm gas. Additionally, disks are very optically thick. For a disk that is 1% of the minimum mass solar nebula, the surface density at 1 au is $\sim 20 \text{ g cm}^{-2}$ (Hayashi 1981). For a solar abundance and Mathis et al. (1977) dust distribution, the disk is optically thick at the mid-infrared wavelengths at which molecular hydrogen emits. Thus only the optically thin atmosphere can be observed. HD is a promising gas tracer owing to its lower upper energy state, far infrared emission lines, and allowed dipole transitions (Bergin et al. 2013; McClure et al. 2016), however, the conversion to a total gas mass is still model dependent. Numerous other gas tracers have been explored for measuring disk masses, but these values are also model dependent and have not been independently validated (e.g., CO; Williams & Best 2014).

Because of the difficulty in measuring gas in disks, the most common avenue to estimate M_{disk} is to convert the observed continuum flux density, f_ν , at a submillimeter frequency ν , to the dust (solids) mass, M_{dust} , then scale M_{dust} by a constant gas-to-dust mass ratio ξ , often assumed to be 100:1, to obtain the gas disk mass, M_{gas} :

$$M_{\text{disk}} \approx M_{\text{gas}} = \xi M_{\text{dust}} = \xi \frac{f_\nu d^2}{B_\nu(T_{\text{dust}}) \kappa_\nu}, \quad (\text{B1})$$

where d is the distance to the source, $B_\nu(T_{\text{dust}})$ is Planck function at the dust temperature T_{dust} , and κ_ν is the dust opacity. Unfortunately, the midplane temperature of the dust has not been measured directly, the opacity of the dust is poorly constrained (Draine 2006), massive disks may be optically thick in mm continuum observations (e.g., Evans et al. 2017), and the gas to dust ratio in the disk has not been robustly measured (cf. Forgan & Rice 2013, Eisner et al. 2016, and Eisner et al. 2018). With these caveats in mind, we have calculated an estimate of the disk mass following this approach.

We provide a submillimeter flux-based M_{disk} estimate (Eqn B1) for the targets listed in Tables 1 and 2 in the following steps. First, we obtain the submillimeter flux density of the sources f_ν from literature (Columns 8 and 10 in Tables 1 and 2, respectively). We adopt measurements at $\lambda = 880 \mu\text{m}$ whenever possible. For all “Well studied NIR disks” we are able to find flux density measurements at wavelengths within a factor of 2 of $880 \mu\text{m}$. Next, we convert all submillimeter flux density measurements to the flux density at $880 \mu\text{m}$, assuming a spectral index $\alpha = 2.4$ (Andrews et al. 2013). For the dust opacity at $880 \mu\text{m}$, we adopt $\kappa = 3 \text{ cm}^2 \text{ g}^{-1}$ (e.g., Beckwith et al. 1990).

For the dust temperature T_{dust} , Andrews & Williams (2005) advocated $T_{\text{dust}} \approx 20\text{K}$ for T Tauri disks, and Henning et al. (1994) advocated 50 K for Herbig disks. Sandell et al. (2011) performed simple model fitting to the SED of a sample of Herbig disks and found $T_{\text{dust}} \sim 30\text{--}70$ K. Andrews et al. (2013) pointed out the T_{dust} dependence on the stellar luminosity L_\star , and suggested scaling T_{dust} as $L_\star^{1/4}$. Pascucci et al. (2016) suggested that the size of the dust disk should also be taken into consideration when estimating T_{dust} .

Here, we introduce another correction factor on T_{dust} based on the outer radius of the disk in submillimeter continuum observations, R_{mm} (Column 12 in Table 2), as where the dust is emitting is also important — a dust ring further from the star is colder than a dust ring closer in, everything else being equal. We scale T_{dust} as

$$T_{\text{dust}} = 30 \left(\frac{L_\star}{38L_\odot} \right)^{1/4} \left(\frac{0.5R_{\text{mm}}}{100\text{AU}} \right)^{-1/2}, \quad (\text{B2})$$

The factor of 0.5 in $0.5R_{\text{mm}}$ is an approximate correction factor meant to identify the radius where the dust temperature is the global average. This is to account for the fact that dust at different radii has different temperature. If the surface density follows a $\Sigma \sim 1/R$ radial profile and the disk extends from $R = 0$ to $R = R_{\text{mm}}$, $0.5R_{\text{mm}}$ is the half-mass radius, i.e., the radius inside which half of the disk mass is enclosed. Equation B2 gives the specific temperature at $R = 0.5R_{\text{mm}}$, not R_{mm} , in a disk; this temperature is considered as a proxy for the average dust temperature in a disk whose outer edge is at R_{mm} . For unresolved submillimeter sources, we adopted the average R_{mm} in resolved sources: 191 AU for Herbig disks and 144 AU for T Tauri disks. This relation is calibrated against a model for HD 163296 (Facchini et al. 2017), and reproduces the midplane temperature produced by several radiative transfer models of both T Tauri and Herbig disks in the literature to within 40% (D’Alessio et al. 1998; Dullemond & Dominik 2004; Dong 2015; Andrews et al. 2016).

Another simple scaling for estimating the disk mass comes from the stellar accretion rate (Hartmann et al. 1998). The stellar accretion rate declines roughly as $t^{-3/2}$; thus the mass remaining in the disk is $M_{\text{disk}} = 2\dot{M}_\star t_{\text{age}}$. Because stellar accretion rates are time variable by a factor of ~ 3 , the mass estimate of an individual disk is uncertain by at least this factor. However, for an unbiased ensemble of disks, the mean mass of the disks is a reasonable estimate. For targets in our volume-limited Herbig IMS sample (Table 2), we conservatively estimate t_{age} to be at least 2 Myr based on the HR diagram (Figure 3).

C. Accretion Rate of Herbig Stars in Table 2

Measuring the accretion rate on to Herbig Ae/Be (HAeBe) stars is complicated by the fact that the stellar photosphere is bright at ultraviolet wavelengths. Thus the contrast between the accretion luminosity and stellar photosphere is low (e.g., Muzerolle et al. 2004). To address this challenge, several groups have calibrated the veiling of the Balmer jump against various emission line diagnostics for stars with the greatest ultraviolet contrast. In an X-Shooter survey of 91 Herbig Ae/Be stars, Fairlamb et al. (2015, 2017) have calibrated the luminosity of 32 emission lines against the accretion luminosity as inferred from the veiling of the Balmer jump.

We recalculated the accretion rates for all sources to obtain a self-consistent set of values. We adopted the accretion luminosity for our sources from the measurement of the Balmer discontinuity when this measurement was available as it is the most direct measure of stellar accretion. When the Balmer discontinuity was not available, we used the luminosity of Br γ or H α ($L_{\text{Br}\gamma}$, $L_{\text{H}\alpha}$) to calculate the accretion luminosity (Fairlamb et al. 2017, Table 2):

$$\log L_{\text{acc}} = (4.46 \pm 0.23) + (1.30 \pm 0.09) \log L_{\text{Br}\gamma}, \quad (\text{C1})$$

$$\log L_{\text{acc}} = (2.09 \pm 0.06) + (1.00 \pm 0.05) \log L_{\text{H}\alpha}. \quad (\text{C2})$$

We prioritized Br γ over H α because it is less sensitive to corrections for both reddening and photospheric absorption.

There are two caveats to keep in mind concerning the measurement of the stellar accretion rate of HAeBes. Firstly, it is not exactly clear how HAeBes accrete. While young A/B stars do not have the convective envelopes believed to play a key role in sustaining the kG magnetic fields observed among their later type counterparts, there is some evidence of magnetospheric accretion (Guimarães et al. 2006; Cauley & Johns-Krull 2014). If magnetospheric accretion controls the star/disk interface, it is likely through higher order field components. However, the conversion of the veiling of the Balmer discontinuity to an accretion luminosity relies on an assumption about the energy in the accretion column (F) and the filling factor (f ; Muzerolle et al. 2004). Neither is well constrained directly for HAeBes. Adopting values that reproduce the observations for T Tauris stars may not be appropriate for these higher mass analogs. Secondly, early type stars with metal poor photospheres, in particular the λ Boo stars, show a UV excess (Murphy & Paunzen 2017). Folsom et al. (2012) and Kama et al. (2015) found a relatively high fraction of HAeBes in their samples (up to $\sim 50\%$) showing the λ Boo pattern to varying degrees. If this effect is common among the targets in our sample, it is possible that \dot{M}_* have been systematically overestimated. Future work to account for the uncertainty in F and f , as well as the effect of the photospheric abundance, will improve our understanding of the stellar accretion rate of these systems.

The luminosities collected from the literature were rescaled using the distances available from Gaia Collaboration et al. (2016) when they were available. Conversion of equivalent width measurements of the HI lines to line luminosities requires correction for the veiled equivalent width of photospheric absorption,

$$W_{\text{circ}} = W_{\text{obs}} - W_{\text{phot}} 10^{-0.4\Delta m} \quad (\text{C3})$$

where W_{obs} is the equivalent width of the emission line, W_{phot} is the equivalent width of the photospheric line, W_{circ} is the equivalent width of the circumstellar emission, and Δm is the excess broadband emission above the stellar photosphere (Rodgers 2001). The equivalent widths of the photospheric features were taken from Fairlamb et al. (2017) when available. For stars not included in their study, stars with matching temperatures and gravities were used to infer the photospheric equivalent width. The veiling in the K-band was determined by the dereddened color excess, $E(V - K_s)$. The intrinsic colors were taken from Pecaut & Mamajek (2013). For the sources where H α was used, the extinction at 6563\AA was inferred from $E(B - V)$, $R_V=5$, and the reddening law presented in Mathis (1990).

The stellar accretion rate is proportional the accretion luminosity so that,

$$\dot{M} = \frac{L_{\text{acc}} R_{\star}}{GM_{\star}}, \quad (\text{C4})$$

where R_{\star} is the stellar radius and M_{\star} is the stellar mass. The stellar parameters were taken from the Siess et al. (2000) pre-main sequence evolutionary tracks and tabulated in Table 2.

D. Comment on Individual Systems

Stars for which the determination of the stellar parameters were not straight forward are discussed in detail. We also comment on the scattered light imaging observations of the AB Aur and HD 100546 disks.

AB Aur ALMA revealed a two-arm spiral structure inside $0''.4$ in the AB Aur disk in CO emission (Tang et al. 2017). This structure was however not well revealed in NIR scattered light (Hashimoto et al. 2011). We conservatively consider the disk to have only multiple weak arms on $\sim 1''$ scale in scattered light.

HR 811 This star was included in a survey of the SED of Herbig Ae/Be stars by Malfait et al. (1998). The SED only reveals an infrared excess longward of $20\mu\text{m}$ leading them to

conclude that this is a Vega-type system. Folsom et al. (2012) included this source in their survey of abundances among Herbig Ae/Be stars, noted the lack of strong optical emission lines, and found that the star had a solar abundance pattern (see also Fossati et al. 2009). We infer the luminosity for this source from the published photometry (Høg et al. 2000) adopting the distance from Gaia Collaboration et al. (2016) and arrive at $L_{\star}=87L_{\odot}$. This value for the luminosity places the star below the early-MS ($127 L_{\odot}$), thus we adopt the stellar mass and radius for a star of this temperature on the zero age main sequence (ZAMS).

V892 Tau There is not parallax measurement for this heavily extinguished source, thus we adopt the average distance to Taurus (Vieira et al. 2003). We adopted the effective temperature ($T\sim 11,000$ K). and luminosity ($L_{\star}=40 L_{\odot}$) from Hernández et al. (2004), and found that the star is slightly below the ZAMS ($49 L_{\odot}$). Given the uncertainty in the distance and reddening correction, this is consistent with a location on the ZAMS, and the mass and radius we adopt for this star reflect that position.

MWC 758 To calculate the accretion rate of this source, we adopted the observed equivalent width of $\text{Br}\gamma$, stellar temperature, and luminosity reported in the literature (Donehew & Brittain 2011; Beskrovnaya et al. 1999; Andrews et al. 2011, respectively). We rescaled the luminosity reported by Andrews et al. (2011) from the distance adopted in that work (200 pc) to the updated distance provided by Gaia Collaboration et al. (2016) (151 pc).

PDS 201 We infer the luminosity for this source from the published photometry (Ducati 2002) adopting the distance from Gaia Collaboration et al. (2016) and arrive at $L_{\star}=9.5L_{\odot}$.

HD 56895 We infer the luminosity for this source from the published photometry (Høg et al. 2000) adopting the distance from Gaia Collaboration et al. (2016) and arrive at $L_{\star}=11.7L_{\odot}$.

HD 97048 We adopt the effective temperature determined by Fairlamb et al. (2015) and rescale the luminosity using the distance provided by Gaia Collaboration et al. (2016). We find $L_{\star}=36 L_{\odot}$ which falls below the zero age main sequence (ZAMS) for a temperature of 10,500 K for the Siess evolutionary tracks. We assume the temperature is the more reliable parameter, so we scale the luminosity so that the star falls on the ZAMS. We adopt $M_{\star}=2.5M_{\odot}$ and $R_{\star}=1.8R_{\odot}$.

HIP 54557 We infer the luminosity for this source from the published photometry (Høg et al. 2000) adopting the distance from Gaia Collaboration et al. (2016) and arrive at $L_{\star}=20.9L_{\odot}$. This source is under luminous by a factor of two. The spectral type was taken from Houk & Cowley (1975). They assign a quality flag of 2 (one a 1-4 scale where 1 is the best). This rating indicates that “the spectra may be slightly under or over-exposed, or slightly overlapped”. It is not clear what uncertainty is appropriate for the inferred stellar temperature. To remain consistent with our other targets, we adopt the stellar mass and radius for a source on the ZAMS.

HD 100546 We adopt the effective temperature determined by Fairlamb et al. (2015) and rescale the stellar luminosity using the updated distance provided by Gaia Collaboration et al. (2016). We find $L_{\star}=25 L_{\odot}$ which falls below the ZAMS for a temperature of 9,750 K for the Siess evolutionary tracks. We assume the temperature is the more reliable parameter, so we scale the luminosity so that the star falls on the ZAMS. We adopt $M_{\star}=2.3M_{\odot}$ and $R_{\star}=2.6R_{\odot}$. Follette et al. (2017) showed that processing a total intensity image of a modestly inclined disk with a small number of spiral arms with Angular Differential Imaging (ADI) techniques may increase the number of arms by breaking them into pieces. The arms seen in the HD 100546 disk may be susceptible to this effect.

PDS 389 There is no parallax measurement reported for this source, so we adopt the distance used by Vieira et al. (2003) based on its cluster membership ($d=175$ pc). We find $L_{\star}=9 L_{\odot}$ which falls below the ZAMS ($14 L_{\odot}$) for a star with this effective temperature (8700 K). The reddening for this source is significant ($B-V=1.87$; Vieira et al. 2003), and uncertainty in the reddening correction likely accounts for our underestimate. We adopt the stellar mass and radius for a source on the ZAMS.

PDS 395 We adopt the effective temperature from Fairlamb et al. (2015), and rescale the luminosity based on the updated distance found from Gaia Collaboration et al. (2016). This star falls 30% below the ZAMS. The origin of this discrepancy is not clear.

HD 141569 Historically, HD 141569 has been included among Herbig Ae/Be stars (e.g., The et al. 1994). It shows H I emission lines, has an extended disk in scattered light (e.g., Weinberger et al. 1999), and a MIR excess (e.g., Malfait et al. 1998). However this IR excess is with a factor of a few of β Pic (Clampin et al. 2003) indicating that it may straddle the transition from gas rich accretion disk to debris disk (e.g., Mawet et al. 2017). This makes the stellar accretion rate inferred from the $H\alpha$ emission, $10^{-8}M_{\odot}\text{yr}^{-1}$ surprising (Mendigutía

et al. 2017a). One solution to this puzzle is comes from the fact that HD 141569 is rotating near its break up velocity and the H I emission is double peaked (Brittain et al. 2007). This situation is consistent with a picture of the H I emission arising from a decretion disk rather than accretion disk. Because the dust disk around the star is optically thin, stellar radiation may sculpt the morphology of the dust leading to the observed rings and spiral structure (e.g., ?). Thus, we exclude this star from our sample.

PDS 80 We adopt the effective temperature from Fairlamb et al. (2015), and rescale the luminosity they report based on the updated distance found from Gaia Collaboration et al. (2016). This star falls 15% below the ZAMS. The origin of this discrepancy is not clear.

HIP 80452 We infer the stellar temperature from the reported spectral type and the luminosity from reported photometry (Høg et al. 2000). The reddening indicates that this source lies behind 1 mag of extinction. We find $L_{\star}=16 L_{\odot}$ which is 16 % below the ZAMS. This discrepancy is likely due to uncertainty in the conversion from a color excess to extinction measure. We adopt the stellar parameters for a star on the ZAMS.

IRS 48 For the effective temperature and stellar luminosity adopted for this source, we find that it falls far below the ZAMS. The extinction towards this source is quite high, ($A_V=11.5$; Brown et al. 2012), so the uncertainty in the extinction correction dominates the uncertainty in the stellar luminosity. We assume the the effective temperature is correct and adopt the stellar mass and radius that places this star on the ZAMS.

HIP 81474 We infer the luminosity for this source from the published photometry (Høg et al. 2000) adopting the distance from Gaia Collaboration et al. (2016) and arrive at $L_{\star}=78.1 L_{\odot}$.

51 Oph We infer the luminosity for this source from the published photometry (Ducati 2002) adopting the distance from Gaia Collaboration et al. (2016) and arrive at $L_{\star}=147.9L_{\odot}$. 51 Oph is a rapidly rotating A0 star (Jamialahmadi et al. 2015) with a minimal FIR excess (Thi et al. 2013). It is not clear whether this small excess is due to a very flat and thus cold disk or a very compact ($R_{\text{out}} \sim 10 - 15$ au disk; Thi et al. 2013). Interferometric observations of 51 Oph indicate that the photosphere is highly flattened due to the large rotational velocity of the star and that $H\alpha$ arises from a geometrically thin Keplerian disk.

As it is possible that this star is a post-Main Sequence object with a decretion disk rather than accretion disk, we exclude it from our sample.

HD 163296 We adopt the effective temperature from Fairlamb et al. (2015), and rescale the luminosity they report based on the updated distance found from Gaia Collaboration et al. (2016).

HD 169142 The spectral type designation of this source has ranged from B9-mid-F in the literature. This is a face-on star rotating near its break-up velocity (Grady et al. 2007) resulting in a significant deformation of the star and resultant temperature gradient from the stellar pole to the equatorial region of the star. As part of their study of λ Boo stars, Murphy & Paunzen (2017) find $T=6700\pm 322$ K and $\log L_*/L_\odot=0.78\pm 0.03$. We adopt these values to estimate the stellar mass and radius from the Siess et al. (2000) evolutionary tracks.

TY CrA This is a heavily extinguished B9 star ($A_V=1.9-3.0$; Ducati 2002). The star falls 14% below the ZAMS which can be accounted for by uncertainty in the reddening correction. We adopt the stellar parameters for a star of this temperature on the ZAMS.

T CrA There is no parallax measurement of this source, so we adopt the distance to this star forming region (130 pc; Vieira et al. 2003). The spectral type is adopted from The et al. (1994). The uncertainty in the spectral type and luminosity is uncertain. Additionally, the proper reddening correction is uncertain. The star is highly variable, thus we select the photometry for which the B and V were acquired contemporaneously (Zacharias et al. 2012) and arrive at $B-V=0.975$. For a spectral type of F0, this implies $E(B-V)=0.66$. The extinction ranges from 2.1 - 3.3 for $R_V=3.1-5.0$. For a temperature of 7200 K, the stellar luminosity is underestimated by a factor of 4. The origin of this discrepancy is unclear, though it is likely due to underestimating the extinction to the source. We adopt the stellar parameters for this star assuming that it falls on the ZAMS.

E. Coordinates of Sources

#	Object	RA	Dec
1	HR811	02 44 07.35	-13 51 31.31
...	LkH α 330	03 45 48.28	+32 24 11.87

Table E.2 continued from previous page

#	Object	RA	Dec
...	FN Tau	04 14 14.59	+28 27 58.06
2	V892 Tau	04 18 40.62	+28 19 15.51
...	RY Tau	04 21 57.41	+28 26 35.54
...	UX Tau	04 30 04.00	+18 13 49.44
...	LkCa 15	04 39 17.80	+22 21 03.48
...	GM Aur	04 55 10.98	+30 21 59.54
3	AB Aur	04 55 45.85	+30 33 04.29
...	SU Aur	04 55 59.39	+30 34 01.50
4	MWC 480	04 58 46.27	+29 50 36.99
5	PDS 178	05 24 01.17	+24 57 37.58
6	MWC 758	05 30 27.53	+25 19 57.08
7	CQ Tau	05 35 58.47	+24 44 54.09
...	V1247 Ori	05 38 05.25	-01 15 21.70
8	PDS 201	05 44 18.79	+00 08 40.40
9	HD 56895	07 18 31.79	-11 11 34.94
...	TW Hya	11 01 51.91	-34 42 17.03
10	HD 97048	11 08 03.31	-77 39 17.49
11	HIP 54557	11 09 50.02	-76 36 47.72
12	HD 100453	11 33 05.58	-54 19 28.55
13	HD 100546	11 33 25.44	-70 11 41.24
...	DZ Cha	11 49 31.84	-78 51 01 1
14	HD 104237	12 00 05.09	-78 11 34.57
15	PDS 141	12 53 17.22	-77 07 10.61
...	PDS 66	13 22 07.54	-69 38 12.22
...	PDS 70	14 08 10.15	-41 23 52.5
16	PDS 389	15 14 47.05	-62 16 59.73
17	SAO 206462	15 15 48.45	-37 09 16.04
18	PDS 395	15 40 46.38	-42 29 53.54
19	HD 141569	15 49 57.75	-03 55 16.34
...	IM Lupi	15 56 09.18	-37 56 06.12
20	PDS 76	15 56 40.02	-22 01 40.00
21	HD 142527 A	15 56 41.89	-42 19 23.27
...	J1604-2130	16 04 21.66	-21 30 28.4
22	PDS 78	16 06 57.95	-27 43 09.79
...	Sz 91	16 07 11.59	-39 03 47.54

Table E.2 continued from previous page

#	Object	RA	Dec
23	HR 5999	16 08 34.29	-39 06 18.33
24	PDS 80	16 13 11.59	-22 29 06.62
...	RX J1615.3-3255	16 15 20.23	-32 55 05.10
25	HIP 80425	16 24 59.15	-25 21 17.98
...	DoAr 28	16 26 47.42	-23 14 52.2
...	SR 21	16 27 10.28	-24 19 12.74
26	IRS 48	16 27 37.19	-24 30 35.03
27	WLY 1-53	16 27 49.87	-24 25 40.2
28	HD 148352	16 28 25.16	-24 45 01.00
29	HIP 81474	16 38 28.65	-18 13 13.71
30	MWC 863	16 40 17.92	-23 53 45.18
31	AK Sco	16 54 44.85	-36 53 18.56
32	51 Oph	17 31 24.95	-23 57 45.51
33	HD 163296	17 56 21.29	-21 57 21.87
...	V4046 Sgr	18 14 10.47	-32 47 34.50
34	HD 169142	18 24 29.78	-29 46 49.33
35	TY CrA	19 01 40.83	-36 52 33.88
36	T CrA	19 01 58.79	-36 57 49.93

Table E.2:: SIMBAD coordinates (ICRS coord. (ep=J2000)) of the sources in Tables 1 and 2, ranked by RA. The first column is the number of Herbig objects in Table 2, if applicable.